Cyclical water vapor sorption-induced structural alterations of mine roof shale

Ang Liu [a], Shimin Liu [a,*], Rui Zhang [b], Guijie Sang [c], Kaiwen Xia [d]

[a] Department of Energy and Mineral Engineering, G³ Center and Energy Institute, The Pennsylvania State University, University Park, PA 16802, USA
[b] Chemical Sciences Division, Oak Ridge National Laboratory, Oak Ridge, TN 37831, USA
[c] Department of Civil and Environmental Engineering, University of Strathclyde, Glasgow, UK
[d] Institute of Geosafety, School of Engineering and Technology, China University of Geosciences (Beijing), Beijing 100083, China

ABSTRACT

Understanding the nanoscale structural changes of shale in an unsaturated gas-water-shale system can shed light on the underlying mechanisms on water retention-induced shale deterioration. The simplified hypothesis here is that pore-scale shale structure can be passively altered by pore deformation/failure under cyclical water vapor treatments and can be described by a partially saturated effective stress law. Cyclical water vapor sorption tests were conducted on dried and water-saturated shale powders prepared by a hand-crushing (larger particle size) method and a cryogenic ball-milling (smaller particle size) method. Techniques including XRD, FESEM-EDS, and nanoindentation were used to provide evidence that the nano-porous shale is highly heterogeneous in nano-to micro-scale. The sorption curves of both samples with initial water-saturation treatments are higher than the raw samples, indicating enhanced sorption capacities in the treated samples. The degree of hysteresis among eight cycles (five cycles on raw sample and three cycles for treated sample) for both samples exhibit significant differences at low relative humidities, namely lower than ~0.6. Very slight differences were observed among eight cycles when the relative humidity was higher than 0.6. An obvious decrease in the effective diffusion coefficients is observed in the treated samples compared to the raw samples, which is attributed to the physical alterations induced by the initial drying of water-saturated sample. *In situ* SANS data for shale at elevated relative humidity conditions suggest that the decrease in the scattering contrast between rock solid matrix and pores can be attributed to water capillary condensation. This occurs mainly in pores with radii smaller than ~8.3 nm but larger than ~1.25 nm and at a relative humidity of ~59%. The capillary condensation continuously takes place in larger pores as the relative humidity increases to ~87%. The results can ultimately provide the data for analyzing the interactions within an unsaturated air-water-shale system.

1. Introduction

Large-scale subsurface projects, including those for oil and gas extraction, for geological carbon sequestration, for energy storage and for building nuclear waste repositories, require comprehensive evaluation and assessment of the properties of the host formation rocks (Moghadam et al., 2020). Geological formations in contact with the atmosphere are often partially saturated, that is, the pore/fracture systems contain water and at least one other fluid. In deep geological formations the fluids are often gas-water, oil-water, or gas-oil-water mixtures (Cheng, 2020).

During hydraulic fracturing, in addition to the water naturally existing in hydrocarbon-bearing shale formations, large volumes of water are injected to create fracture networks that enable commercially viable hydrocarbon production rates (Engelder et al., 2014). Water retention in the porous shale and the resultant shale-water interactions play important roles in determining the transport behaviors of gas-bulk water or gas-water vapor mixtures under full or partial water saturation conditions. Water imbibed in fractures can migrate into nanoscale pores due to an elevated capillary pressure, reducing the pore gas interconnectivity to open fracture networks for effective gas production. If the gas pressure drawdown is not large enough to overcome this capillary effect, water blockage can occur and gas becomes trapped inside pore voids impairing the cumulative gas production (Ghanbari and

Dehghanpour, 2015).

Aqueous phases and sedimentary rocks are usually thought to interact in two ways: physically through abrasion and migration and chemically through dissolution and recrystallization (Barsotti et al., 2021). However, a fundamental understanding of shale-water interactions in shale gas reservoirs remains a challenging issue because the complexity of the shale pore structure, the variations in shale compositions and their heterogeneities, and the complexity of shale-water interactions (among many other factors) add other phenomena to the possible interactions. (Clarkson et al., 2013; Sang et al., 2020).

Micropores (< 2 nm) and mesopores ($2 - 50$ nm) in nanoporous shale are undoubtedly important in gas production because they constitute a large fraction of the shale porosity for gas/water storage and transport (Gu et al., 2015). The fractal shape and the structural integrity (inter-connectivity) of pores are essential factors in determining gas and water deliverability through shales (Bolton et al., 2000; Schaefer et al., 2012; Slatt and O'Brien, 2011) which are passively altered with the coupled effects of fluid transfer *via* flow and the *in situ* stress evolution. During continuous gas/brine production, a shale formation is partially saturated with brine and the relative humidity in the pores dynamically varies with time. During this process, the capillary pressure caused by water condensation or water retention plays a critical role in determining the tendency of the formation to imbibe water, its relative permeability, and the mechanical integrity of the rock (Moghadam et al., 2020). An improved understanding of this water condensation behavior—and the resultant changes of capillary pressure within the unsaturated shale due to the variations in relative humidity—is a prerequisite in interpreting the role of water retention in the shale structural alterations at pore-scale (Sang et al., 2020).

In the case of water imbibition/water retention in nanoporous shale, following the Kelvin equation, capillaries become spontaneously filled with water at the relative humidity (R_h) (Yang et al., 2020):

$$R_h = exp(-2\sigma/k_B T d\rho_N) \tag{1}$$

where T is temperature, K; σ is the surface tension of water at temperature T, mJ•m^{-2}; k_B is the Boltzmann constant; $\rho_N \approx 3.3 \times 10^{28}$m^{-3} is the number density of water; d is the diameter of the meniscus curvature, $d = h/cos\theta$, where h is the diameter of cylindrical pores or the distance of parallel walls constituting the slits, nm, and θ is the contact angle of water on the surface of solid skeleton. For capillary condensation to occur at relative humidity (R_h) considerably below 100%, Eq. (1) dictates that d must be comparable to $2\sigma/k_B T\rho_N \approx 1.1$ nm. As an example, under typical ambient R_h of 40–50%, water is expected to condense in slits with $h < 1.5$ nm and cylindrical pores with diameters $<$ 3 nm, if the contact angle θ is close to zero. Naturally, stronger confinement is required for capillaries involving less hydrophilic materials because of the increase in contact angle θ.

It is a general consensus that the Kelvin equation (Eq.(1)) remains accurate for menisci with $d \geq 8$ nm and can also describe condensation phenomena in hydrophilic pores as small as 4 nm in diameter (Charlaix and Ciccotti, 2010; Honschoten et al., 2010). Yang et al. (2020) studied capillary condensation in atomic-scale capillaries with the smallest dimension down to less than four angstroms. The macroscopic Kelvin equation can also be readily applied to both strongly and weakly hydrophilic materials by substituting the characteristics of bulk water. It is evident that the water condensation phenomenon is omnipresent under ambient conditions in shale because the pore sizes are distributed from micron-to-sub nano meters or $2\sigma/k_B T\rho_N$. Elevated capillary pressure resulting from capillary condensation can cause considerable deformation (Altabet et al., 2017; Gor et al., 2017; Gruener et al., 2009; Schoen and Günther, 2010). The capillary pressure (P) at the condensation transition can be expressed as:

$$P = 2\sigma cos\theta/h \tag{2}$$

Accordingly, a negative capillary pressure above the relative humidity of capillary transition evolves with R_h, which can be given as (Charlaix and Ciccotti, 2010; Honschoten et al., 2010; Powles, 1985):

$$P = k_B T \rho_N ln(R_h) \tag{3}$$

In partially saturated gas-water-shale systems, the pore pressure can be separated into three dynamic forces acting through the gas and water phases, namely, the pore-gas (u_a)/pore-water (u_w) pressures acting on the dry/wetted surface portions of the solid skeletons and the total suction being comprised of matric and osmotic components acting along the gas-water interfaces (Fredlund, 1991). In the case of unsaturated gas-water-shale systems where the osmotic component is negligible, the pore-water pressure can be visualized as being highly negative—as much as 10,000 atm (Fredlund, 1991). Matric suction is the difference between the pore-gas pressure and the pore-water pressure, ($u_a - u_w$). It can be calculated by combing Eq.(2) or Eq.(3) and the pore-gas pressure (Fredlund et al., 2012, 1994). The matric suction is a stress state variable in the gas-water-shale system, influencing the evolution of effective stress on the solid skeleton (Lu, 2008). Bishop's effective stress approach for describing matric suction involves a modified form of Terzaghi's classic effective stress formulation for an unsaturated gas-water-shale system. The effective stress acting on the solid skeleton can be written as (Lu and Likos, 2006):

$$\sigma_e = \sigma_t - u_a + \chi(u_a - u_w) \tag{4}$$

where σ_e is the effective stress; σ_t is the total stress; χ is the effective stress parameter, which is generally considered to vary between zero and one and is a function of the degree of pore-water saturation, $\chi = \alpha S_w$. S_w is water saturation, which is defined as the ratio of water volume in pores to the total pore volume. A value of χ equal to zero corresponds to the perfectly dry condition. When the value of χ equals one, it corresponds to the saturated condition. Based on Eq. (4), water retention in nanoconfined pores exhibits 'weakening' effects on the solid skeleton of shale (Poulsen et al., 2014). In the case of shale gas production, because of continuous gas/brine production, the shale formation is partially saturated with brine and the relative humidity in the pores varies with time. The changes in capillary pressure because of water condensation or water retention (see Eqs. (2) and (3)) will influence the state of the effective stress acting on the solid skeleton of the shale (Eq. (4)). Considering this, a simplified statement of the hypothesis of this study is that the pore-scale shale structure can be passively altered by pore deformation/failure that can be described by the partially saturated effective stress law. Using this hypothesis, the conceptualization of the changes of suction stress in the unsaturated air-shale-water system, and its influences on the deformation of nanoporous shale are illustrated in Fig. 1. To mimic the tortuous pore pathways in shale, the ideal two-dimensional confinement created by parallel walls separated by a nanoscale distance h_0 has been assumed herein (Fig. 1 (a)). Driven by the gradient of relative humidity between the inlet and outlet, the water vapor molecules diffuse into the nanoscale confinement by a combination of the Knudsen diffusion attributed to the flow of free water vapor molecules and surface diffusion of the adsorbed water layer (Choi et al., 2001), as illustrated in Fig. 1 (a). For low relative humidity, capillary pressure cannot be generated due to the absence of meniscus curvature. The solid wall and the water molecules are usually thought to interact in two ways: physically through abrasion and migration and chemically through dissolution and recrystallization (Barsotti et al., 2021). As surface diffusion continues, the adsorbed layer of water vapor molecules can form a meniscus curvature due to water condensation at the critical relative humidity condition, and this can be evaluated using the Kelvin equation (Eq. (1)). At this condensation transition, the meniscus is caused by the surface tension and the diameter of the meniscus curvature (d) depends on the contact angle of water on the surface of the solid wall for a known confinement with a distance of h_0. As described by Eq. (2), a negative capillary pressure is generated at the condensation transition and the parallel walls could be deformed by the amount δ_c
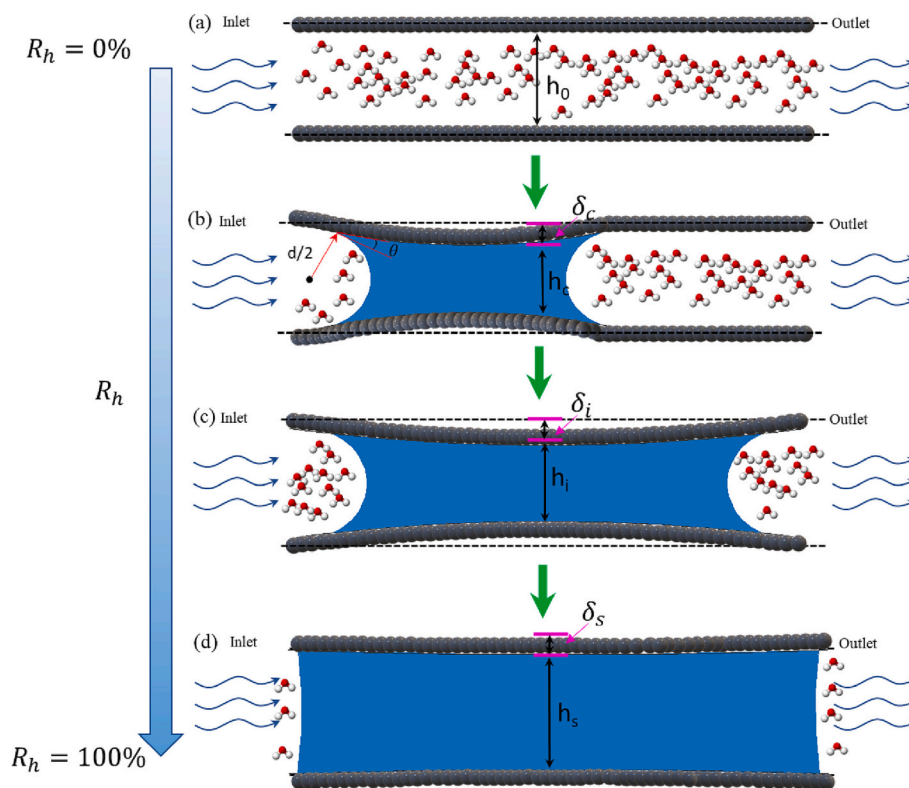
Fig. 1. Water vapor sorption-induced deformation of nanoporous shale. (a) low R_h condition; (b) capillary transition at critical R_h; (c) beyond the condensation point as R_h is continuously increased, the confinement is continuously enhanced; (d) as R_h closes to 100%, the confinement recovers to its original state.

(Fig. 1 (b)). As R_h exceeds the condensation point, the meniscus extends outside the capillaries, and its curvature becomes progressively smaller to match the external R_h. Accordingly, the negative capillary pressure above the condensation transition evolves with R_h and is given by Eq. (3) (Fig. 1 (c)). As R_h approaches 100%, the value of $P \propto ln(R_h) \approx (R_h - 1)$ is expected to linearly approach zero (Yang et al., 2020). The optimized nanoscale confinement is expected to approximately recover to its original state (Fig. 1 (d)).

In Fig. 1, the ideal two-dimensional confinement is assumed to be elastically deformed due to the changes in capillary pressure. The capillary pressure can range from hundreds to thousands of bars depending on the surface tension, contact angle, the pore radius, relative humidity, *etc.* For the heterogeneous shale, the stiffness/strength of the solid matrix varies with the mineral composition and the pores, cracks, and cavities—which obviously do not terminate at the scale of several nanometres but may extend below even 1 nm. With water vapor desorption, the elevated capillary pressure acting on the solid matrix is expected to increase the effective stress based on Eq. (4). Considering common rock failure criteria such as the Mohr-Coulomb and the Hoek-Brown criteria, nano−/micro−/macro-scale structure changes under this dynamic effective stress condition are expected. Furthermore, under drying, the cyclic changes of the effective stress within the unsaturated air-water-shale system can initiate shale structural changes. These changes can alter the volume of the pore space and the interconnectivity of the gas or water transport pathways.

This study employs a series of techniques to indirectly quantify water vapor sorption-induced deformation(s) of nanoporous shale. The techniques include X-ray diffraction (XRD), field emission scanning electron microscopy - energy dispersive spectroscopy (FESEM-EDS), nanoindentation, laser diffraction, low-temperature nitrogen adsorption (LTNA) and CO_2 adsorption. In addition, *in situ* small-angle neutron scattering (SANS) experiments, and cyclical water vapor sorption tests using Dynamic Vapor Sorption (DVS) were used to probe the pore-scale structural evolution and test the proposed hypothesis. Again, the

hypothesis is that the gas accessibility of shale matrix is passively altered through pore damage/collapse and structural failure attributable to local humidity gradient variations and/or mineral-water interactions. In this study three things were attempted: 1) to provide collective and comprehensive evidence of the occurrence of the capillary condensation transition; 2) to determine to what extent the water holding capacity and the kinetic behavior of water vapor transport are altered; and 3) to evaluate the potential failure /damage and collapse within the formation(s) because of cyclical changes in the relative humidity boundary. The results of the study provide pore-scale insights into the water condensation behavior, which is of practical significance in understanding the role of water on hydrocarbon extraction, CO_2 trapping during CO_2 sequestration, wellbore stability, injection induced-seismicity, roof control in underground coal mining, and the formation of gas hydrates—as well as other related phenomena.

2. Materials and methods

2.1. Sample collection, preparation and characterizations

The raw shale samples were collected from the immediate roof over a coal seam at a surface mine in the state of Indiana, USA. In the laboratory, two thin sections and several sizes of powders were prepared from just one shale block (cubic shape with ~5 cm length) for material consistency (See Table 1). The first thin section (T1) was cut perpendicular to the bedding planes and had dimensions of ~150 μm (T) × 2 cm (W)× 2 cm (L) and was then mounted on a quartz slice for *in-situ* SANS measurements (Sang et al., 2020). The second thin section (T2), having dimensions of ~0.5 cm (T) × 2 cm (W)× 2 cm (L), with arbitrary cutting directions, was used for mechanical nanoindentation tests, and imaging and elemental analysis using FESEM-EDS (Section S1 in the Supporting Information). To quantify the mineralogical compositions using XRD, powder sample P1 was pulverized, using hand grinding, to pass through a 325-mesh sieve (Fig. S1 and Section S2 in the Supporting Information).

Table 1
Sample preparation method, denotation, and characterization techniques.

Sample shape	Size (*T × *W× *L)	Denotation	Characterization technique
Thin slice section	~150 μm × ~2 cm× ~2 cm	T1	*in situ* SANS characterization
	~ 0.5 cm × ~2 cm× ~2 cm	T2	Nanoindentation; FESEM-EDS
Powder	>325 mesh	P1	XRD
	80–100 mesh	P2	DVS; LTNA; CO_2 adsorption; particle size analyzer
	Cryogenic ball-milling	P3	DVS; LTNA; CO_2 adsorption; particle size analyzer

*T denotes thickness; *W denotes width; *L denotes length.

A second powder sample (P2) was prepared using the same method as sample P1. Further, a third sample P3 was prepared using a cryogenic ball-milling method using CryoMill (Retsch Inc.). An integrated cooling system built into the CryoMill instrument ensures that the grinding jar is continually cooled with liquid nitrogen before and during the grinding process. A liquid nitrogen-cooled environment can prevent frictional heating of the powder sample and helps maintain the pristine nanopore structure. A maximum of 20 ml of the hand-crushed shale powders were put into the grinding jar. A 5 Hz vibrational frequency was used for pre-cooling, and three cycles with 5 min for each cycle and a 30 Hz vibrational frequency were used for the cryo-mill sample preparation. The particle size distributions of samples P2 and P3 were determined using a laser diffraction method (Section S3 in the Supporting Information). Powder samples P2 and P3 were used for cyclical water vapor DVS tests (five cycles), LTNA tests, and CO_2 adsorption tests. In addition, some of raw samples P2 and P3 were saturated with liquid water for 15 days and then used for cyclical DVS tests (three cycles). The *in-situ* SANS experiments on sample T1 were performed in a controlled *in situ* water vapor environment using a CHRNS 30 m SANS instrument at the NIST Center for Neutron Research (NCNR). All the other experiments were conducted at Pennsylvania State University.

Figure S2 shows a comparison of the volume, surface area and particle number distributions of sample P2 and P3 as measured by the laser diffraction method. The particle sizes of both sample P2 and P3 have relatively broad distributions from ~0.3 μm to ~240 μm for sample P2, and from ~0.3 μm to ~20 μm for sample P3. The volume distribution of sample P2 has a broader range with two peaks, one peak is caused by particles with a size at ~15 μm, the other peak occurs due to the existence of larger particles with a size of ~100 μm. But for sample P3, only one narrower peak shape shifted to a smaller particle size of ~2 μm. The surface area distributions of samples P2 and P3 showed similar peaks. The surface area distribution has a peak in particles of sample P3 for particle sizes <1 μm, and two similar peaks formed a broader peak for sample P2 for particle sizes range from ~0.3 μm to ~3 μm. Overall, powder samples prepared using the hand-crushing method are less homogenous than the smaller powders generated using the cryogenic ball-milling method. Particle size is reduced for both volume and surface area in sample P3.

2.2. In situ SANS experiment and cyclical water vapor sorption test

2.2.1. In situ SANS experiment

For the SANS experiments, detailed experimental information can be found in our previous study (Sang et al., 2020). An *in situ* environmental chamber with controlled temperature and relative humidity and containing a 60% D_2O to 40% H_2O mixture (by weight) was used. The scattering length density in the liquid of 60% D_2O and 40% H_2O mixture is approximately 3.6×10^{-10} cm^{-2}. A total range of the scattering vector (Q) of 0.0015 Å^{-1} < Q < 0.3 Å^{-1} was covered with the 30 m SANS instrument. This was accomplished by choosing sample-to-detector distances of 1 m, 4 m, 13 m, and 13 m (with a lens). During the *in-situ* SANS

measurements, the relative humidity was controlled by two mass flow controllers by adjusting the ratio of dry N_2 gas to saturated water vapor, which was generated by a bubbler inserted into the liquid D_2O/H_2O mixture. The temperature in the humidity chamber was maintained at ~23 °C to avoid the appearance of water droplets induced by condensation. The first step for the SANS test was conducted under drying condition through flooding dry gas, followed by elevated relative humidity and then back to drying condition to make one complete cycle.

2.2.2. Cyclical water vapor sorption test

The DVS Intrinsic (Surface Measurement Systems Ltd.) instrument is designed to accurately measure the mass changes of a sample under different relative humidities. The mechanism behind the DVS instrument is a gravimetric method based ultra-sensitive recording microbalance. The ultra-sensitive recording microbalance is capable of measuring changes in sample mass with an accuracy of one ppm. As air with a known relative humidity passes over the sample, the changes in the sample mass are continuously recorded. A known relative humidity is generated by accurately mixing dry (dry N_2 stream) and saturated-vapor gas flows (wetting N_2 stream containing 100% humidity) in the desired proportions, using precision mass flow controllers. In this study, the water vapor adsorption and desorption of samples P2 and P3 were measured in a relative humidity range from 0 to 0.95 and then back to 0 to make one complete cycle. Five complete cycles were measured. The equilibrium state of water vapor adsorption and desorption under different relative humidities is defined to be when the mass change is less than or equal to 0.002% per minute and is maintained stable for ten minutes. The average of the last three data points was taken as the final equilibrium value (Liu and Liu, 2021).

3. Theoretical models

3.1. Water vapor sorption isotherm

The monolayer adsorption model, a Langmuir-type model, is commonly used and explains the sorption mechanisms and behavior well (Langmuir, 1916). In a Langmuir-type sorption model, the surface of the adsorbent is assumed to be homogeneous and there is a maximum surface concentration of absorbate that is absorbed on it in a monolayer pattern. Additional assumptions are that the adsorption sites are identical and mutually independent, and that each site can accommodate only one molecule. This Langmuir-type model is appropriate for describing the mono-molecular coverage of the water vapor sorption process. But the existence of multilayer adsorption of water vapor cannot be described by the Langmuir-type equation. The Brunauer-Emmett-Teller (BET) model is widely used to sorption isotherm of water vapor sorption (Brunauer et al., 1938). However, the BET model is only valid in the range of relative humidity below 0.35 (Charrière and Behra, 2010). The BET model has been continuously improved (Charrière and Behra, 2010), and one improved model is the Guggenheim, Anderson, and De Boer (GAB) model (Anderson, 1946; de Boer, 1953; Guggenheim, 1966), which is applicable over a more broad range of relative humidity. Subsequently, the Dubinin-Serpinsky (DS) model assumes that water molecules firstly adsorb on energy privileged centers (*i.e.*, oxygen functional groups) and those adsorbed molecules are capable of providing secondary adsorption centers for water-water interactions through hydrogen bonds (Dubinin et al., 1955). However, one drawback of the DS model is that its assumption lacks of saturation of the secondary adsorption centers (Furmaniak et al., 2008). In this work, water vapor is presumed to be initially adsorbed on the primary adsorption sites and to have a monolayer distribution in the presence of hydrophilic functional groups due to their strong binding energy with water molecules. Subsequently, those adsorbed water molecules that occupy primary sites are considered as the secondary centers for multilayer adsorption (*i.e.,* formation of water aggregates or clusters) which is followed by a capillary condensation stage. Strictly, those

multilayers can start to form even before full coverage by the monolayer. Likewise, the capillary condensation at a heterogeneous surface begins to occur before the completion of multilayer adsorption. Thus, for the sake of simplification of the modeling, in this study primary adsorption is considered to be equivalent to monolayer adsorption and secondary adsorption to both the multilayer adsorption and capillary condensation.

The Langmuir-type sorption model for water vapor sorption with respect to relative humidity can be written as (Langmuir, 1916):

$$m_{pri} = \frac{m_L R_h}{R_L + R_h} \quad (5)$$

where m_{pri} is the primary adsorption of water vapor at specified relative humidity, g/g; m_L is the maximum water vapor uptake corresponding to complete monolayer coverage, g/g; and R_L is the relative humidity at which the measured adsorption content is equal to ½ m_L, dimensionless.

To accommodate multilayer adsorption and capillary condensation, the phenomenological Dubinin-Serpinsky approach was introduced in the mid-1950s to describe the formation of water aggregates or clusters on energy-privileged sites acting as primary adsorption centers. The Dubinin-Serpinsky model can be written as (Dubinin et al., 1955):

$$m_{sec} = \frac{m_0 c k R_h}{1 - c k R_h} \quad (6)$$

where m_{sec} is the secondary adsorption of water vapor at a given specified relative humidity, g/g; m_0 is the surface concentration of the energy at privileged hydrophilic adsorption centers, g/g; c is the ratio between the rate constants of adsorption and desorption, dimensionless; k is a dimensionless constant, which represents the loss of secondary sites during adsorption. In the original Dubinin-Serpinsky approach, k is treated as a part of c and is equal to one.

Ideally, all the primary adsorbed water molecules can become secondary adsorption centers and are available for multilayer formation of water aggregates or clusters. The isothermal curve of water vapor sorption over the full range of relative humidity is the summation of the primary adsorption and secondary adsorptions and can be expressed as (Furmaniak et al., 2008):

$$m = m_{pri} + m_{sec} = \frac{m_L R_h}{(R_L + R_h)(1 - c R_h)} \quad (7)$$

where m is the gravimetric water content, g/g.

3.2. Estimation of diffusion coefficient based on the unipore model

The kinetics of water vapor flow can be described by various models including the linear driving force mass-transfer model, the unipore, and bidisperse models. The unipore model quantifies the apparent transport behavior of fluid in porous media using a representative diffusion coefficient, instead of focusing on the contributions of different flow regimes in different types of pores. Water diffusion in shale can be estimated from the unipore diffusion model (Charrière and Behra, 2010; Duan, 2018; Sang et al., 2020), which is derived from Fick's second law of diffusion. The Fick's diffusion equation in spherical coordinates takes the following form (Liu et al., 2022):

$$\frac{\partial C}{\partial t} = \frac{1}{r^2} \frac{\partial}{\partial r} \left(D_w r^2 \frac{\partial C}{\partial r} \right) = D_w \left(\frac{2}{r} \frac{\partial C}{\partial r} + \frac{\partial^2 C}{\partial r^2} \right) \quad (8)$$

where C and D_w are the adsorbate concentration and constant diffusion coefficient respectively, mol/cm^3 and cm^2/s; and r is the particle radius. Given a constant concentration at the surface of the spherical particle, the solution of Eq. (8) has the following form (Liu et al., 2022):

$$\frac{M_t}{M_\infty} = 1 - \frac{6}{\pi^2} \sum_{n=1}^{\infty} \frac{1}{n^2} exp \left(-\frac{D_w n^2 \pi^2 t}{r_p^2} \right) \quad (9)$$

where M_t and M_∞ are the total mass of water adsorbed at time t and at the equilibrium state, respectively; r_p is the radius of the shale particle in this work, mm. Based on Eq. (9), under initial dry condition (~ 0% R_h), the residual water desorbs and the mass of the sample decreases to a constant value which is taken to be the mass of the dry sample (or reference mass). Then water vapor adsorption and desorption isotherms for the studied shale samples can be calculated by taking the difference between the reference mass and the equilibrium mass of shale samples at a given relative humidity. In this study, for samples P2 and P3, the effective diffusion coefficients ($\frac{D_w}{r_p^2}$) were estimated over a range of relative humidities using the unipore model (Eq. (9)).

4. Results and discussions

4.1. Mineralogical composition

The mineralogical composition of the shale sample was analyzed by XRD, as summarized in Table 2. The shale sample contains ~17.7% quartz, ~29.3% illite, ~8.6% montmorillonite, ~5.0% muscovite, ~11.6% halloysite, ~3.1% pyrite and ~ 3.3% dolomite. The amount of total organic carbon is ~21.4%.

The fabric features of the shale and the 64 indents created by the indenter were identified by FESEM, as shown in Fig. 2(a). The distribution of mesopores (larger than 10 nm) and macropores and mineral content can be observed in the grayscale image. By combing the elemental analysis results with EDS (Fig. 2 (b) and (c)) and the XRD results in Table 2, the localized mineralogical compositions can be roughly confirmed. As examples, the main mineral at the region of indent 15 can be identified as quartz due to the presence of oxygen and silicon elements in the spectrum and the mineral compositions in Table 2, as shown in Fig. 2(d). The spectrum of indent 57 only includes the elements oxygen and carbon indicating that organic carbon matter is the main component in this region. The localized Young's moduli determined from the force-displacement curves of the 64 indents created by nanoindentation are plotted in Fig. 3. The Young's moduli determined from the location-dependent indents differ mainly because of the mineralogical compositions and the local structural characteristics. Based on the 64 indents, the calculated Young's modulus ranges from ~3.34 GPa to ~38.64 GPa with the maximum Young's modulus located at indent 15, which is enriched with quartz, and the minimum one located at indent 57 which is mainly filled by organic carbon matter. The Young's modulus and uniaxial compressive strength of the bulk sample were measured using a core-scale specimen with a diameter of 50 mm and a length of 100 mm. They were 3.7 GPa and 82.1 MPa, respectively. The Poisson's ratio of the bulk sample is ~0.25, which was used to calculate the Young's moduli in Fig. 3.

4.2. CO₂ sorption and LTNA

Figure 4 shows the sorption isotherms for samples P2 and P3 as measured by LTNA and CO_2 adsorption. The CO_2 sorption isotherms of both samples are Type I isotherms according to the IUPAC classification (Thommes et al., 2015). The isotherms show a rapid rise in the sorption amount with increasing relative pressure up to a limiting value, which is consistent with Langmuir-type isotherm The maximum sorption capacity of sample P3 is obviously higher than that of sample P2, especially at higher partial pressure, as shown in Fig. 4(a).

The surface area, pore volume, and pore size distribution (PSD) information for the shale samples can also be estimated using density function theory (DFT) (Section S4 in the Supporting Information). The isotherms of LTNAs for both samples P2 and P3 followed the pattern of Type IV isotherms with a sharp uptake in the saturated vapor pressure, which indicates the frequently-encountered multilayer physical adsorption in nano-porous solids (Thommes et al., 2015). The initial Langmuir-type adsorption part represents the formation of an adsorbed

Table 2
Mineralogical compositions of shale sample based on XRD analysis (weight %).

Compositions	Quartz	Illite	Montmorillonite	Muscovite	Halloysite	Pyrite	Dolomite	TOC[a]
Content (%)	17.7	29.3	8.6	5.0	11.6	3.1	3.3	21.4

[a] TOC stands for total organic carbon, which was measured from the ultimate analysis based on ASTM standards.

monolayer, while the remainder of the curve represents multilayer adsorption as is typical for shale. It shows that both the monolayer and multilayer adsorption capacities in sample P3 are higher than sample P2, as shown in Fig. 4(b). Type II isotherm can be used to calculate a BET surface area, a BJH pore volume, a BJH pore size distribution, and a BJH average pore diameter. In Fig.S3 (a), the PSDs measured by CO_2 sorption are very similar. For sample P3 the curve shifted to a somewhat smaller pore width indicating the reduced nanoscale pores in sample P3. In Fig. S2, it shows that sample P3 contains smaller particles. Compared with sample P2, more nanoscale pores are present in sample P3, which is consistent with the results from Fig.S2. The PSDs measured by the LTNA method in samples P2 and P3 are very similar and an obvious increase in the pore volumes is observed in sample P3. The mesopore size range of ~2 nm to ~100 nm in samples P2 and P3 are very similar, while the quantity of pores in sample P3 is obviously higher than that in sample P2. In addition, it was found that there was a more than two times increase in the BET surface area determined from LTNA in sample P3 compared to sample P2, and 1.5 times increase in BET surface area measured by CO_2 sorption. A 3.2-fold increase in the BJH pore volume and 1.17 times increase in the DFT pore volume from sample P2 to sample P3 was measured using the LTNA and CO_2 sorption methods, respectively. Both the BET surface area and pore volume increase in the finer sample P3 (Fig.S2). BET average pore diameter slightly decreased from 9.280 Å to 6.942 Å while BJH average pore width increased from 77.124 Å to 103.978 Å for sample P3 (Table 3), indicating micropores become slightly smaller while macro−/mesopores become larger after cryogenic ball mill. In addition, based on the IUPAC classification, the adsorption hysteresis can be classified, and it is widely accepted that there is a correlation between the shape of the hysteresis loop and the texture (*e.g.*, pore size distribution, pore geometry and connectivity) of a porous material (Thommes et al., 2015). The adsorption hysteresis in Fig. 4(b) exhibits Type H3 hysteresis loop, which reflects that the shale sample contains developed slit-shaped pores.

4.3. Water vapor sorption isotherm and the degree of hysteresis

Figure 5 shows the isotherms of the cyclical DVS tests for samples P2 and P3 and the fitting curves based on Eq. (7). Based on Eq. (7), the fitting curves agree well with the experiment data with a goodness-of-fit factor (R-squared) over 0.99 in the regression analyses. The fitting parameter m_L represents the maximum water vapor uptake corresponding to complete monolayer coverage, and fitting parameter R_L represents the critical relative humidity during the Langmuir-type adsorption stage. The sorption constant c indicates the multilayer sorption capacity. The isotherms of water vapor in both samples are Type II isotherms according to the IUPAC classification (Thommes et al., 2015) (Fig. 5). The initial parts of the sorption isotherms represent the formation of an adsorbed monolayer, while the remainder of the sorption curves represent multilayer adsorptions as for porous shale. In Fig. 5, the sorption curves of both samples P2 and P3 with initial water-saturation treatments are higher than the raw samples P2 and P3, indicating enhanced sorption capacities in the treated samples. For raw samples P2 and P3 without water-saturation treatment with liquid water at the initial time, the adsorption curves are very close in sample P2 (Fig. 5 (a)) among five cycles. A distinct increase in the adsorption curve of cycle 1 to the following cycles was observed for sample P3 in Fig. 5 (c), indicating an obvious change in the water holding capacity. The differences among the desorption curves of the five cyclical tests on sample P3 are also more obvious than those in sample P2.

The changes of sorption capacities among five cyclical tests were quantified through the fitted sorption constants, as shown in Fig. 6. For the changes of sorption capacities caused by cyclical tests, the maximum capacities of monolayer adsorption in raw sample P2 show stable values regressed from the adsorption data, but a continuous decrease in m_L from 0.0333 to 0.0306 was determined from desorption data. The critical relative humidity R_L and the sorption constant c regressed from the adsorption data representing the multilayer sorption capacity over the five cycles do not show obvious variations. But the critical relative humidity R_L regressed from desorption data shows a very distinct decreasing trend, while a slight increase in the sorption constant c is shown. For the raw sample P3, a sharp increase in m_L from cycle 1 (0.0157) to cycle 2 (0.07) is observed based on the adsorption data but a similar decrease in m_L from cycle 1 (0.0298) to cycle 5 (0.0272) is observed. The critical relative humidities and sorption constant c at both the adsorption and desorption stage follow the same trend as sample P2. Overall, the monolayer sorption capacity of raw sample P3 is lower than that of sample P2 does, while the multilayer adsorption capacity exhibits the opposite behavior.

For samples P2 and P3 with water-saturation treatment with liquid water at the initial time, significant changes in sorption isotherms were observed (Fig. 5). The adsorption curves under cyclical tests do not vary obviously in samples P2 and P3 (Fig. 5) but the sorption curves are shifted to higher gravimetric water content compared to raw samples P2 and P3, indicating an obvious change in the water holding capacity. Based on the fitted sorption constants in Fig. 6, sharp increases in both the monolayer sorption capacity m_L and the relative humidity R_L were observed, while an obvious decrease in the sorption constant c occurred. The changes of sorption capacities among the five cyclical tests on raw samples and the three cyclical tests on treated samples can be explained using the hypothesis put forth in Fig. 1. The increase in relative humidity can generate capillary pressures at the condensation transition points in nanoscale pores, as quantified in Fig. 6. For each one of the five or three cycles, the relative humidity R_h ranges from ~0% to ~99%, then back from 99% to ~0%, in a stepwise manner. During the adsorption stage, the capillary pressure would attain its peak at the critical relative humidity R_h (as shown in Eqs. (2) and (3)), then it tends to decrease because the meniscus curvature becomes progressively smaller to match the external R_h. As drying occurs, the nanoscale pores are desaturated under the gradient of relative humidity between the interior and exterior of the powders. During the desorption period, the capillary pressure is supposed to first increase and then disappear at lower relative humidity. Overall, the dynamic capillary pressure passively changed in response to the variations in the external relative humidity. Recalling the effective stress law in Eq. (4) coupling the matric suction caused by capillary pressure, the structural alterations can be caused in both adsorption (wetting) and desorption (drying) stages. The main difference between samples P2 and P3 is the pore size/pore volume distribution. The average pore diameter in sample P3 is smaller than in sample P2 (Fig. 6), and thus it is supposed that the water condensation effects are more obvious in sample P3 in accordance with Eq. (1) and Fig. 1. Raw samples without water treatment (Fig. 5 and Fig. 6) showed an obvious change in sorption capacity from cycle 1 to cycle 2 among the five cycles, which is attributed to the distinct physical alterations in sample P3. As water vapor diffuses into shale powders during cycle 1, the high effective stress resulting from the matric suction (mainly during the desorption stage) acting on the solid skeleton can trigger damage/failure or collapse in regions with 'weak' stiffness. The physical changes accompanying drying during the desorption stage occur more easily than do those during
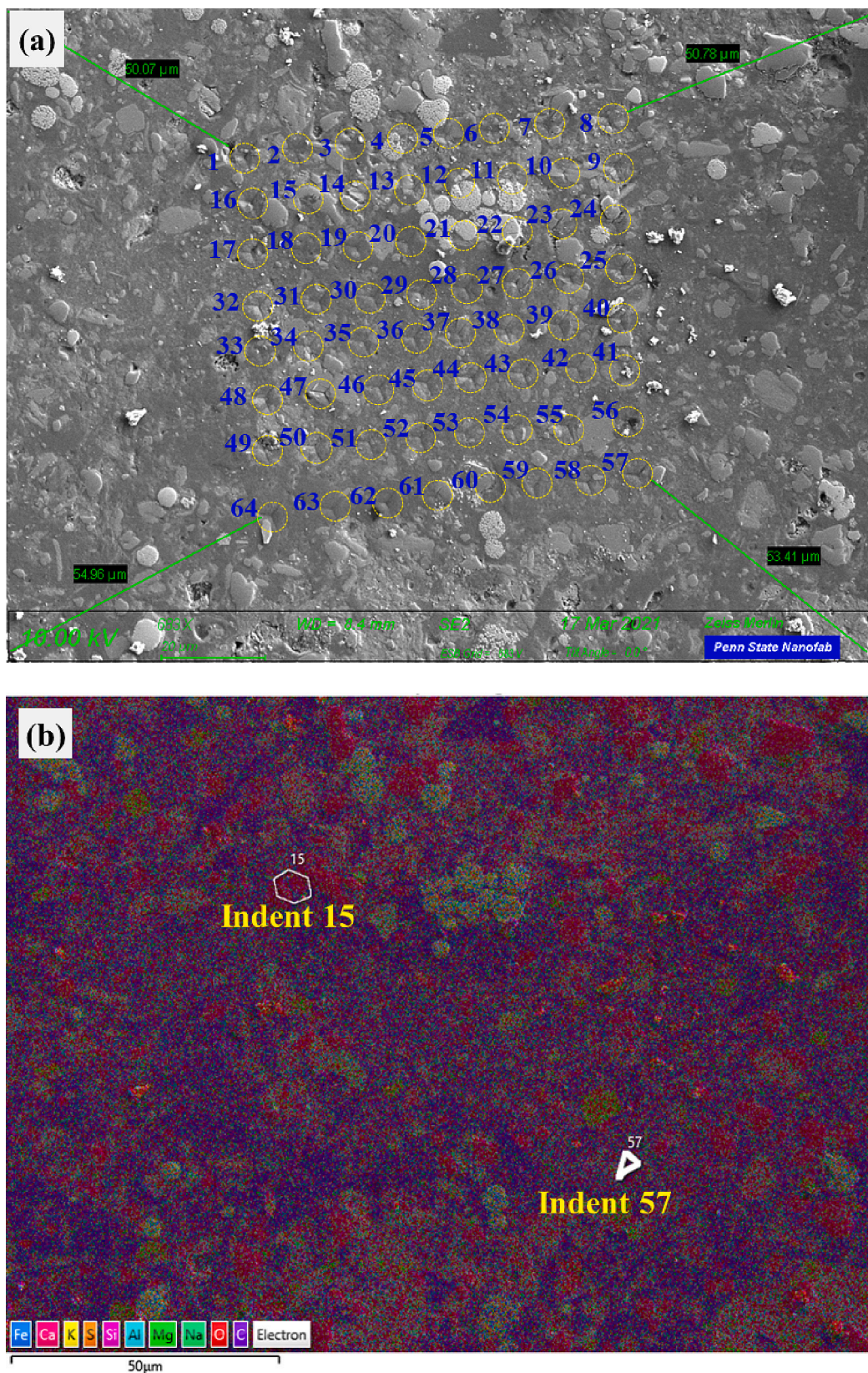
Fig. 2. Nanoindentation and FESEM-EDS results for sample T2.

the adsorption stage, as shown in Fig. 6. As water vapor diffuses into the dry shale, the shale is progressively saturated because of the increase in relative humidity. During this process, the water condensation phenomena first start to occur in nanoscale pores and then extends to larger pores with an increase in relative humidity. In other words, the water condensation phenomena are not omnipresent in most of the
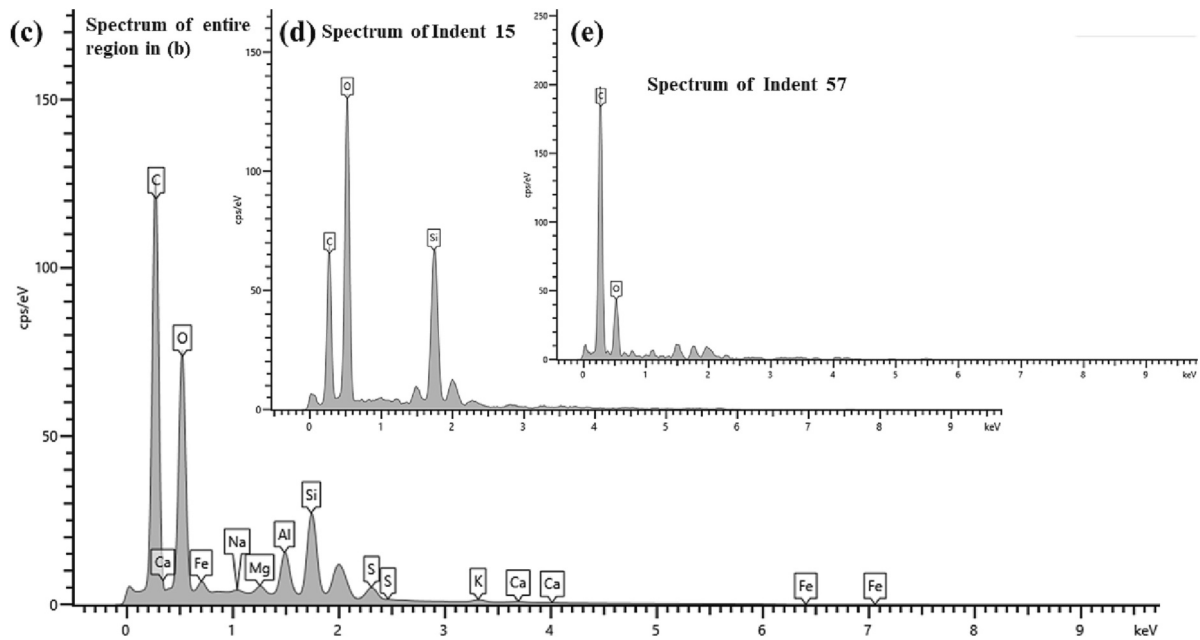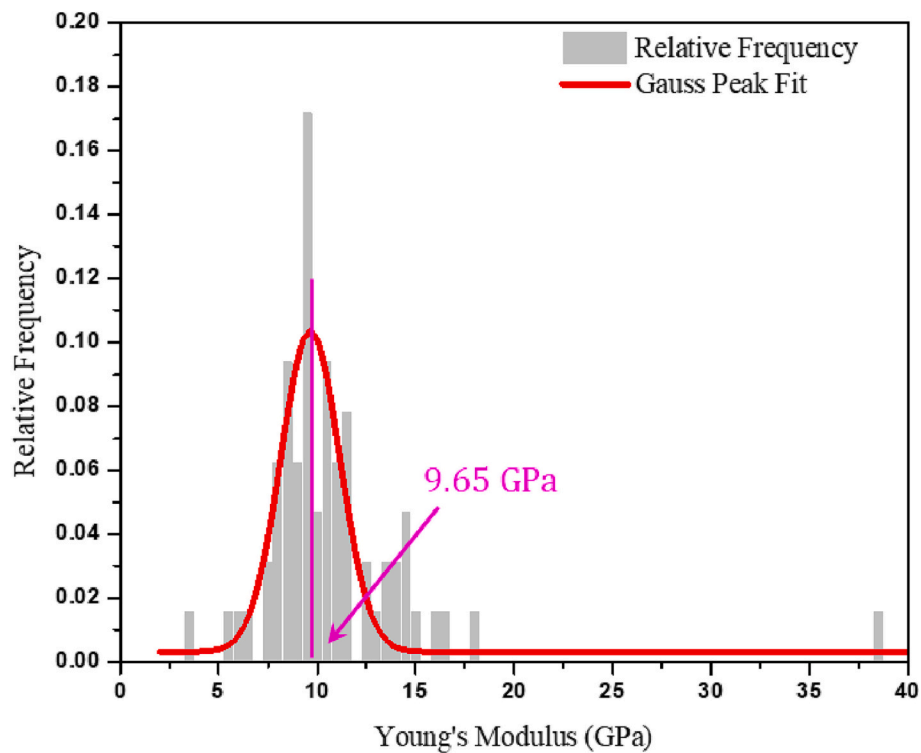
Fig. 2. (*continued*).

Fig. 3. Distribution of Young's moduli obtained from 64 indents on sample T2.

pores, while the opposite is true for the desorption process. As drying occurs, the sample is initially water saturated at ~99% relative humidity, even if the capillary pressure is low under high relative humidity (Eq. (3)), the capillary pressure tends to increase until the condensation transition point. Ideally, all the pores were initially filled with water and the capillary pressures were omnipresent in almost every pore. Typically, the sample is water-saturated at the starting point of desorption and the water-shale interactions occur physically through abrasion and migration and chemically through dissolution and recrystallization (Barsotti et al., 2021). The 'weakening' effect induced by water-shale

interaction can be obvious during the desorption stage because the water is present in almost all locations. This fact makes the changes of sorption capacities at the desorption stage greater than at the adsorption stage. This phenomenon can be evidenced by the cyclic testing results for the samples initially treated with liquid water. As initial drying occurs for the water-saturated samples P2 and P3, the physical alterations can cause obvious changes in the water-holding capacities of the samples and significant jumps in sorption constants were observed—see Fig. 6.

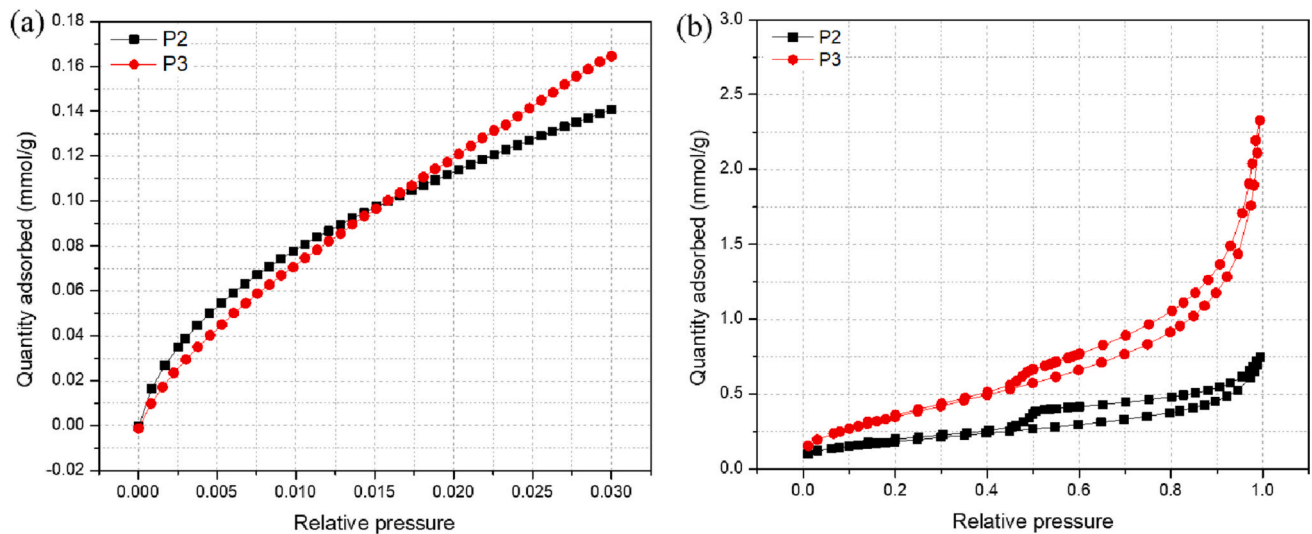The structural changes caused by adsorption and desorption can be

Fig. 4. Comparison of sorption isotherms using low-pressure CO_2 and LTNA. (a) CO_2 sorption; (b) LTNA.

Table 3
Pore volume, surface area, and average pore diameter results.

	LTNA				CO_2 sorption	
	BET surface area (m^2/g)	BET average pore diameter (4 V/A) (Å)	BJH pore volume (10^{-3} cm^3/g)	BJH average pore width (4 V/A) (Å)	BET surface area (m^2/g)	DFT pore volume in pores $\leq$ 10.66 Å (10^{-3} cm^3/g)
P2	14.9863±0.0417	9.280	24.268	77.124	17.2109±0.9057	3.57
P3	30.6854±0.2943	6.942	77.702	103.978	26.4863±2.2468	2.48

reflected through the degree of hysteresis, defined as *Hysteresis degree* $= (m_{de} - m_{ad})/m_{ad}$, where m_{ad} and m_{de} are the gravimetric water content at the same relative humidity during the adsorption and desorption stage, respectively. In Fig. 7, the degrees of hysteresis of both the five cycles on raw samples and the three cycles on treated samples were calculated and plotted. It is shown that the degrees of hysteresis of all cyclic tests increase with relative humidities and peak at relative humidity of ~0.6 to ~0.7. The degree of hysteresis among eight cycles (five cycles on raw sample and three cycles for treated sample) for both sample P2 and P3 exhibit significant differences at low relative humidities, namely lower than ~0.6. Very slight differences were observed among eight cycles when the relative humidity was higher than 0.6. For sample P2 without water-saturation treatment, the degrees of hysteresis of the five cycles tests can be clearly distinguished. Cycle 1 exhibits a lower degree of hysteresis compared with the following four cycles. This is because after cycle 1 typically the desorption process, the structural alterations due to drying effect occur. This phenomenon is even more obvious in smaller pored sample P3. It can be observed that the degree of hysteresis of sample P3 is higher than sample P2. This can be attributed to the smaller pores in sample P3 which enhance the potential for capillary condensation to occur and the associated drying effects. For samples P2 and P3 after water-saturation treatment prior to the cyclical tests, there is no obvious difference between the raw sample and treated-samples. However, the degrees of hysteresis of the three cyclic tests in sample P3 with water treatment have very slight fluctuations among the three cycles but show significant changes compared with the results of five cycles on the raw samples. Interestingly, the degrees of hysteresis of the three cyclic tests in sample P3 with water treatment tend to be close to the values of cycle 4 and cycle 5 in raw sample P3, which may be attributed to the strong physical alterations that had already occurred in the initial drying stage of the treated sample.

4.4. Changes of kinetics behavior of water vapor sorption in shale

Figure 8 shows the effective diffusion coefficients of water vapor in shale as calculated using Eq. (9). During the adsorption stages, the effective diffusion coefficients are R_h-dependent and showed very similar trends in both raw samples and treated-samples. The diffusion coefficients initially increase at relatively low relative humidity but then continuously decrease as the relative humidity progressively reaches ~0.99. Before reaching the peaks, the increase in diffusion coefficients is controlled by the fast diffusion induced by flow of water vapor molecules in the free phase and the surface diffusion controlled by the flow of water molecules in the adsorbed phase. At this stage, the surface diffusion is relatively rapid since enough sorption sites exist on the surface of shale matrix. As the relative humidity increases, surface diffusion dominates the transport of water vapor molecules. However, the sorption sites are occupied with adsorbed water molecules and the surface diffusion process is slowed down. Under higher relative humidity, capillary condensation occurs in most of the pores and the diffusion of water vapor will decrease to its lowest value and finally ceases at the nominal saturated condition. For desorption, the pores are initially filled with nominal liquid water. As drying occurs, the flow of water vapor molecules, especially the adsorbed water molecules in the multilayer, is easy due to the weak bonding between water molecules, thus the initial effective diffusion coefficient is highest at a relative humidity from ~99% to ~90%. After the outflow of water in the multilayer slows, the outflow of adsorbed water is controlled by surface diffusion. With the decrease in relative humidity, the diffusion will slow down due to the strong H-bonding between the water molecules and wall surfaces and the increasing resistance of water outflow from nanoscale pores. Below the condensation transition point, the meniscus curvature disappears and the flow channels for water molecules are fully open and so the diffusion process can become fast. At the final drying stage, the most difficult process is the flow of water vapor from nanoscale pores. The role of the van der Waals forces between the walls in nanoscale pores
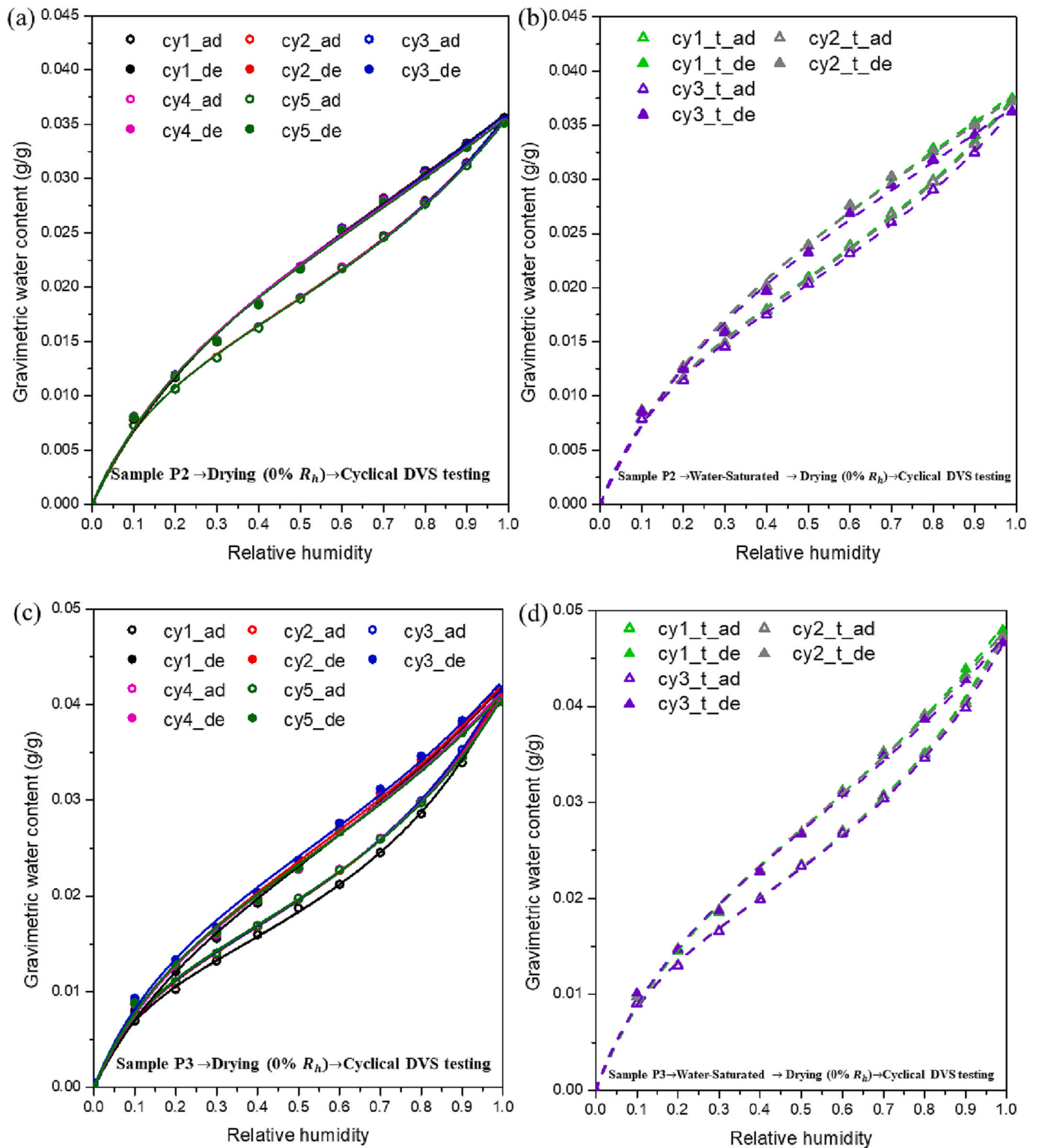
Fig. 5. Isotherms of the cyclical DVS tests for samples P2 and P3. (a) raw sample P2 and (b) sample P2 after water-saturation treatment; (c) raw sample P3 and (d) sample P3 after water-saturation treatment. Points: experimental data; solid lines: fitting curves of raw samples P2 and P3; dash lines: fitting curves of samples P2 and P3 with water-saturation treatment. For simplification, the legend 'cy' is short for 'cycle', the numbers 1, 2, 3, 4, and 5 are cycle numbers, the notation 'ad' and 'de' come from 'adsorption' and 'desorption', respectively, and the notation 't' indicates water-saturation treatment on samples.

becomes significant when the outflow reaches the last one or two layers of water molecules, and this may induce the collapse of the walls (Yang et al., 2020). In Fig. 8, an obvious decrease in the effective diffusion coefficients is observed in the treated samples compared to the raw samples, which is attributed to the physical alterations induced by the

initial drying of water-saturated samples. For larger pored raw sample P2, the diffusion coefficients among the five cycles show very slight difference with each other in the adsorption stage, while an obvious difference is observed in the desorption stage. The finding is consistent with the results in Fig. 7 showing that the desorption is affected more
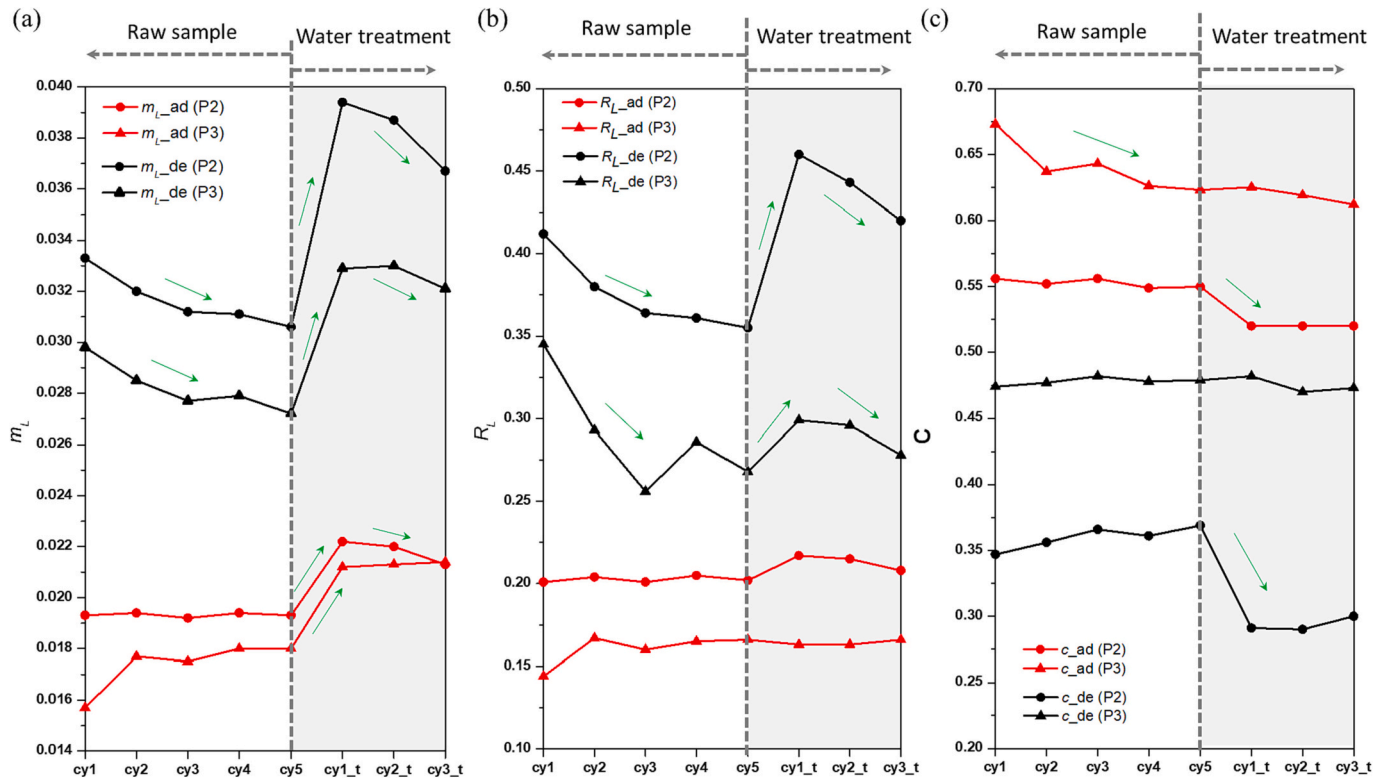
Fig. 6. Comparisons of sorption constants from the fitting results in Fig. 5 based on Eq. (7). (a) constant m_L indicating the maximum capacity of monolayer sorption; (b) constant R_L; and (c) constant c indicating the multilayer sorption capacity.
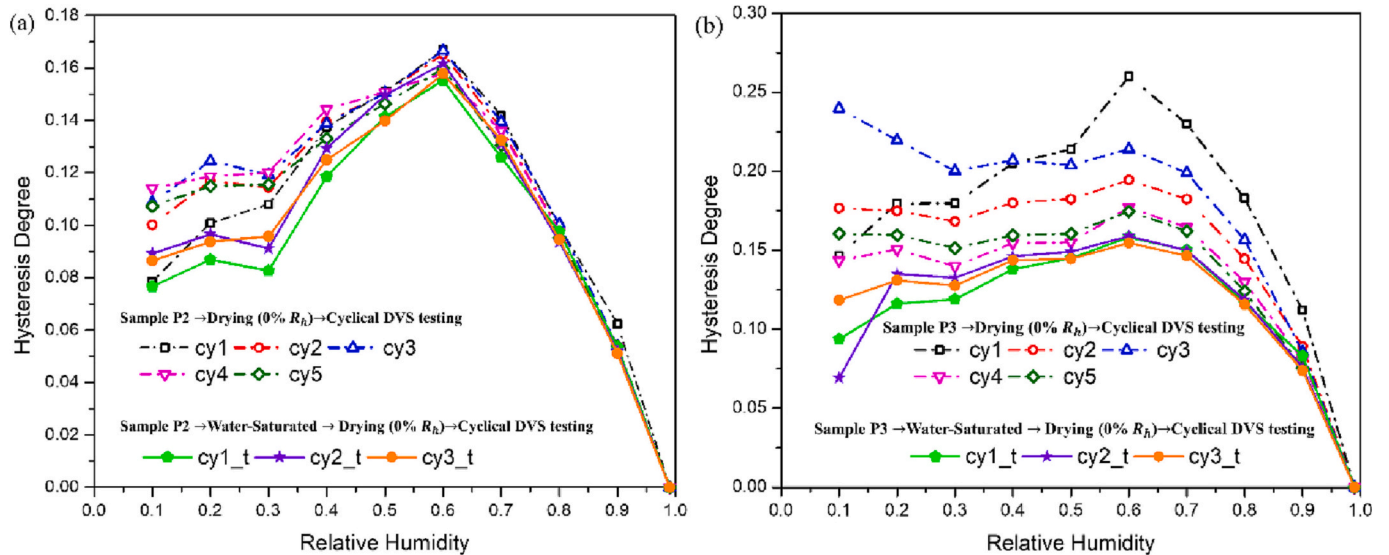

Fig. 7. Comparison of the hysteresis degrees from sorption isotherms in samples P2 and P3. (a) sample P2; (b) sample P3. solid lines: fitting curves of raw samples P2 and P3; dash lines: fitting curves of samples P2 and P3 with water-saturation treatment.

strongly than adsorption under cyclical tests. In smaller pored raw sample P3, the diffusion coefficient in cycle 1 is highest in the adsorption stage but at its lowest value in the desorption stage; all other cycles show similar trends.

4.5. In situ SANS results

For characterizing the pore-scale shale-water vapor interactions, the SANS intensity ($I(Q)$) for a two-phase (shale solid matrix and pore) system can be expressed as follows (Sang et al., 2020):

$$I(Q) = 4\pi \left(\rho_s^* - \rho_p^*\right)^2 \phi(1-\phi) \int_0^\infty r^2 \gamma_0(r) \frac{sinQr}{Qr} dr \qquad (10)$$

where $\left(\rho_s^* - \rho_p^*\right)^2$ is the scatting contrast between shale solid matrix and pores, where ρ_s^* is the scattering length density (SLD) of shale solid matrix and ρ_p^* is the SLD of pores; ϕ is the shale porosity; $Q = 4\pi\lambda^{-1}sin(\theta/2)$ is the scattering vector; λ and θ are the neutron wavelength and the scattering angle, respectively; $\int_0^\infty r^2 \gamma_0(r) \frac{sinQr}{Qr} dr$ is the Fourier transform
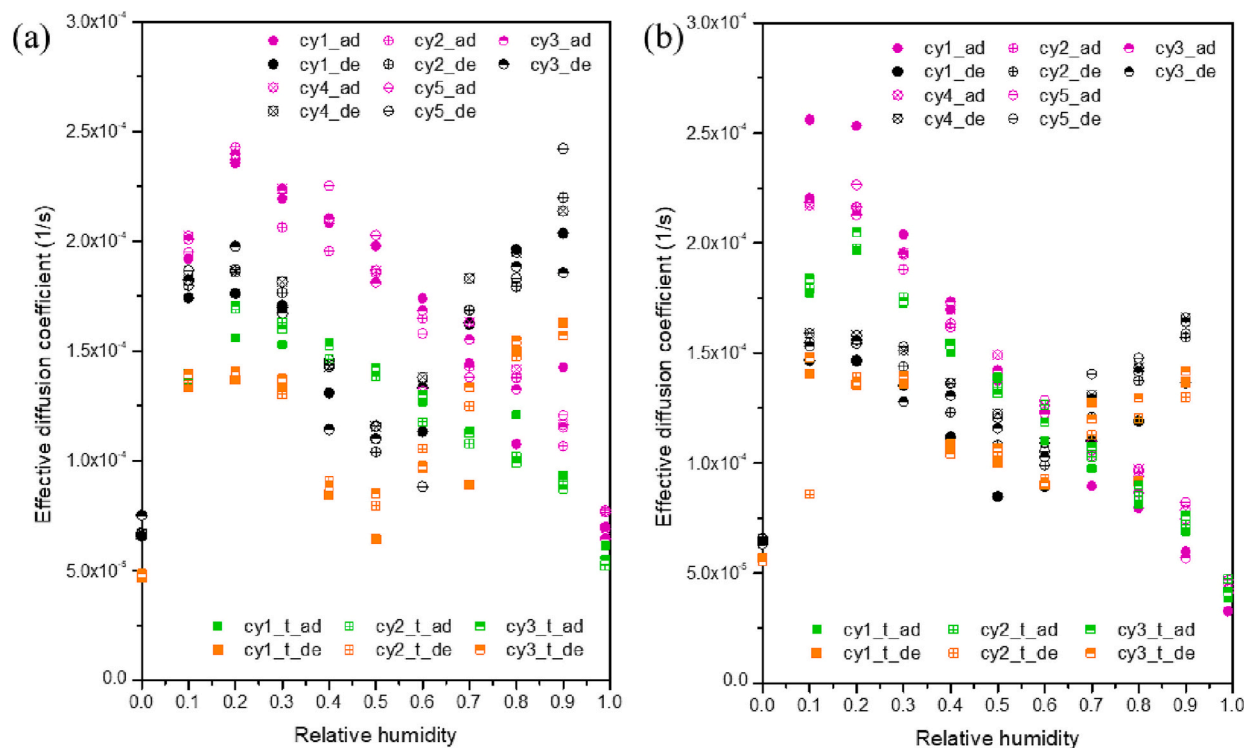
Fig. 8. Effective diffusion coefficients of the cyclical DVS tests for samples P2 and P3. (a) raw sample P2 (magenta and black circle symbols) and sample P2 after water-saturation treatment (green and orange cube symbols); (b) raw sample P3 (magenta and black circle symbols) and sample P3 after water-saturation treatment (green and orange cube symbols). (For interpretation of the references to colour in this figure legend, the reader is referred to the web version of this article.)

of the correlation function $\gamma_0(r)$. Based on Eq. (10), the measured SANS intensity $I(Q)$ in a two-phase shale system is attributed to the scattering contrast $\left(\rho_s^* - \rho_p^*\right)^2$ between the shale solid matrix and pores. Based on the two-phase scattering assumption, pores occupied by the contrast-matching condensed D_2O/H_2O are supposed to increase the SLD of those pores. This suggests that the pores occupied with contrast-matching condensed D_2O/H_2O will not contribute to neutron scattering—rendering the pores neutron transparent. Thus, the degree of water condensation in the pores can be directly quantified by comparing the scattering patterns recovered under dry, then prescribed, humidity conditions. In addition, the pore size can also be correlated with the scattering vector from an empirical relationship (Radliński et al., 2000) as: $r \approx 2.5/Q$, where r is the pore radius of a polydisperse porous medium.

The *in-situ* SANS measurement data of shale sample T1 was documented, as shown in Fig. 9. Fig. 9 (a) and (b) show the effects of elevated relative humidity on the scattering intensities. Compared with the initial dry condition ($R_h \sim 2\%$), the scatting intensity for $R_h \sim 10\%$ remains almost unchanged over the entire range of the scattering vector. The scattering intensity for $R_h \sim 28\%$ also exhibits no changes but a slight decrease at higher values of the scattering vector. A significant decrease in the scattering intensity can be observed for relative humidity at $R_h \sim 59\%$. Typically, with a relative humidity of $R_h \sim 59\%$, it was observed that the scattering intensity exhibits a significant decrease with the scattering vector value range between ~ 0.03 Å^{-1} to ~ 0.2 Å^{-1} (between the green arrows on the figure). This suggests that the decrease in the scattering contrast between rock solid matrix and pores was due to water capillary condensation—mainly in pores with radii smaller than ~ 8.3 nm but larger than ~ 1.25 nm. Further, in pores with those radii, the capillary condensation process was almost complete as the relative humidity increased to $R_h \sim 71\%$ because there were almost no changes in the scattering intensity curves as the relative humidity finally approached $R_h \sim 87\%$. However, this does not mean that the capillary

condensation never occurs in larger scale pores below a relative humidity of $R_h \sim 87\%$. Compared with other relative humidity conditions, it should be noted that there is a slight decrease in scattering intensity with a relative humidity of $R_h \sim 87\%$ at smaller values of the scattering vector, suggesting that the capillary condensation occurs in larger pores.

Figure 9 (c) and (d) show the variations of scattering intensities with the decrease in relative humidity. As the relative humidity decreases from $R_h \sim 87\%$ to $R_h \sim 75\%$, there are almost no changes in the scattering intensity over the entire range of scattering vector values while there are slight increases as the relative humidity decreases to $R_h \sim 62\%$. Compared with all other lower relative humidity conditions ($R_h \sim 38\%$, $R_h \sim 11\%$, and $R_h \sim 1\%$), the scattering intensities at these three relative humidities remain the lowest. Recalling the appearance of the capillary condensation point in Fig. 9 (a) and (b), which is lower than $R_h \sim 59\%$, it seems the disappearance point of capillary condensation was still not reached under these three relative humidity conditions. As the relative humidity continuously moves down to $R_h \sim 38\%$, it is very interesting that the scattering intensity slightly increases in the pores with radii larger than 1.25 nm but smaller than ~ 2.5 nm. Simultaneously, the scattering intensity increases dramatically in the pores with radii larger than 2.5 nm but smaller than ~ 12.5 nm. This suggests that liquified water vapor due to capillary condensation starts to be gasified in pores, first in relatively larger pores, followed by smaller pores. This finding can be further confirmed by comparing the scattering curves among relative humidity conditions of $R_h \sim 38\%$, $R_h \sim 11\%$, and $R_h \sim 1\%$. In Fig. 9 (d), there is a dramatic increase in the scattering intensity in pores with radii larger than 1.25 nm but smaller than ~ 2.5 nm as the relative humidity deceases from $R_h \sim 38\%$ to $R_h \sim 11\%$, which means the capillary condensation starts to disappear in these smaller pores under lower relative humidity conditions. The process is almost complete at a relative humidity of $R_h \sim 11\%$ because there are no significant changes in the scattering intensity curves between relative humidity conditions of $R_h \sim 11\%$ and $R_h \sim 1\%$.
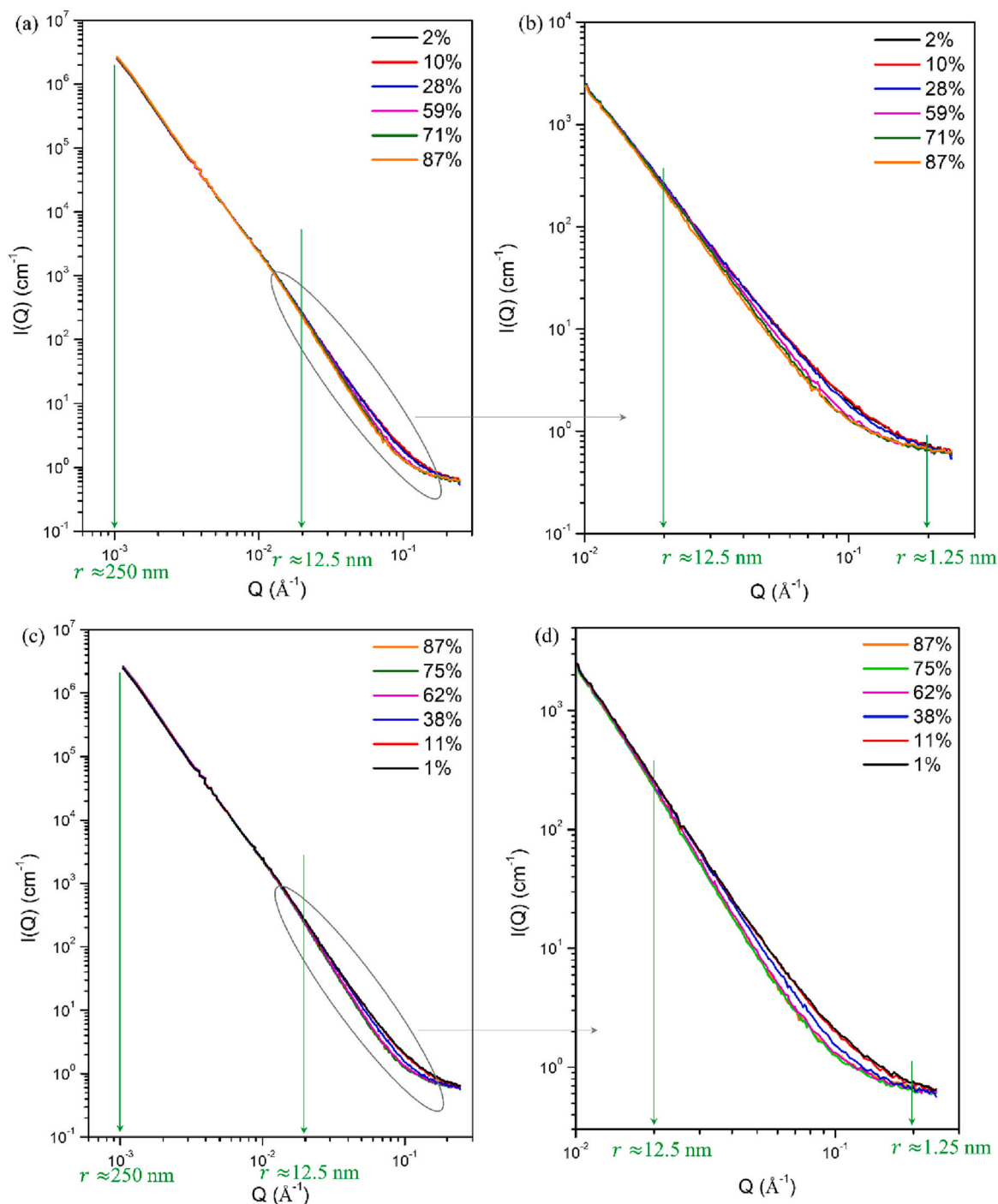
Fig. 9. SANS scattering profiles as a function of the scattering vector Q with elevated relative humidity ((a) and (b)) and degraded relative humidity ((c) and (d)) in Herrin shale.

4.6. Mechanism-based understandings of structural alterations in the unsaturated air-water-shale system

Even though no direct evidence (*i.e.,* FESEM images) that show permanent changes in nanoscale pore structures, there exists indirect evidence from both cyclical water vapor sorption tests and the SANS data were. In Fig. 5, the single isotherm of water vapor sorption cannot reveal permanent changes in nanoscale pore structure because the quantified index is gravimetric water content. The first and last step of one full-cycle water sorption test both have 0% relative humidity, which means water gain and loss during the adsorption and desorption stage will not change the loaded sample weight. Consequently, the single isotherm of water vapor sorption cannot be an indicator of structural alterations during the full cycle. However, if there are structural alterations during the first cycle, then the changes to the isotherms of water vapor sorption during the second cycle (and each subsequent cycle) will be observed because the water sorption capacity is correlated with pore structures. This deviation of sorption isotherms among the cycles can be observed in Fig. 5., especially when the sample was pre-saturated with water. The differences among the later cycles are not as obvious—this is because most of the alterations to weak nanostructures occurred during the early cycles. In section 4.5, the SANS technique is non-destructive,

and SANS data exhibits the statistical number density of pores with certain sizes (*i.e.*, scattering vector) and scattering contrast between pores and surrounding matrix. Supposing there were no structural alterations during the full circle, the change of scattering intensity curve before and after humidity measurements would not be expected. Comparing scattering intensities before and after introduced humidity in the shale sample (Fig.S4), very slight permanent changes can be observed when the scattering vector value is higher than $\sim 0.1 \, \text{Å}^{-1}$.

Based on the combined results using different characterizing techniques, the hypothetical mechanism-based understandings of structural alterations in the unsaturated air-water-shale system are illustrated in Fig. 10. The alterations of water vapor sorption isotherms and diffusivity can be directly measured from the cyclical DVS tests. Techniques including XRD, FESEM-EDS, and nanoindentation were used to provide evidence that the nano-porous shale is highly heterogeneous and anisotropic in nano-to micro-scale mechanical properties. Data from the LTNA, CO_2 adsorption, and SANS measurements were used to confirm the occurrence of capillary condensation in nano- to micro-scale pores in agreement with the Kelvin equation. With this evidence, it can be stated that the pore-scale shale structure can be passively altered by pore deformation/failure in accordance with the partially saturated effective stress law given in Eq. (11).

Typically, shear stresses inside the shale powders would not be expected under hydrostatic pressure conditions, but they can be generated by diffusion-controlled sorption-induced deformation (Liu et al., 2017, 2016) concentrating stress around the nanopores inside the powder. In this study, the hydrostatic pressure should be the partial pressures of water vapor molecules under the different relative humidities. However, the hydrostatic pressure condition cannot be maintained at every region within the powdered shale because of the complex phase changes of water vapor molecules. The phase changes due to adsorbed layers of water molecules and water vapor liquification caused by capillary condensation at high relative humidity conditions can cause

concentrated stress around the nanopore interfaces inside the powder—in accordance with the Kelvin equation. As shown in Fig. 11, the pore distributions and shale heterogeneity can cause uneven transport of water vapor molecules before the final equilibrium is reached at each relative humidity stage. Generally, smaller spaces such as the high-lighted pore throats 'A' and 'B' are more susceptible to capillary condensation than other sites (at the same relative humidity), and therefore stress concentrations can be caused by the presence of the resulting liquid-solid-air interface. As given in the Kelvin equation, the decrease in relative humidity can cause a significant increase in matric suction pressure, which impacts the shear stress acting on the solid shale matrix. Therefore, discussion of the shear stress changes due to the dynamics of matrix suction and the extended Mohr-Coulomb failure envelope for the unsaturated shale-water-air system in the experiment is required.

Following the Bishop's approach, as quantified in Eq. (4), the shear strength may be described by incorporating a modified effective stress expression into the classical Mohr-Coulomb failure criterion:

$$\tau = c' + [(\sigma_t - u_a) + \chi(u_a - u_w)]tan\phi' \qquad (11)$$

where τ is the shear strength; c' is the effective cohesion intercept; and ϕ' is the effective angle of internal friction associated with the net normal stress state variable $(\sigma_t - u_a)$.

Based on Fredlund and Morgenstern's independent stress state variable approach, the net normal stress $(\sigma_t - u_a)$ and matric suction $(u_a - u_w)$ are treated independently in terms of their roles in the mechanical behavior of the unsaturated air-water-shale system. From Eq. (11), the shear strength may be described as (Lu and Likos, 2006):

$$\tau = c' + (\sigma_t - u_a)tan\phi' + (u_a - u_w)tan\gamma \qquad (12)$$

where γ is the effective angle of internal friction associated with the matric suction $(u_a - u_w)$, $tan\gamma = \chi tan\phi'$. The first two terms comprise the
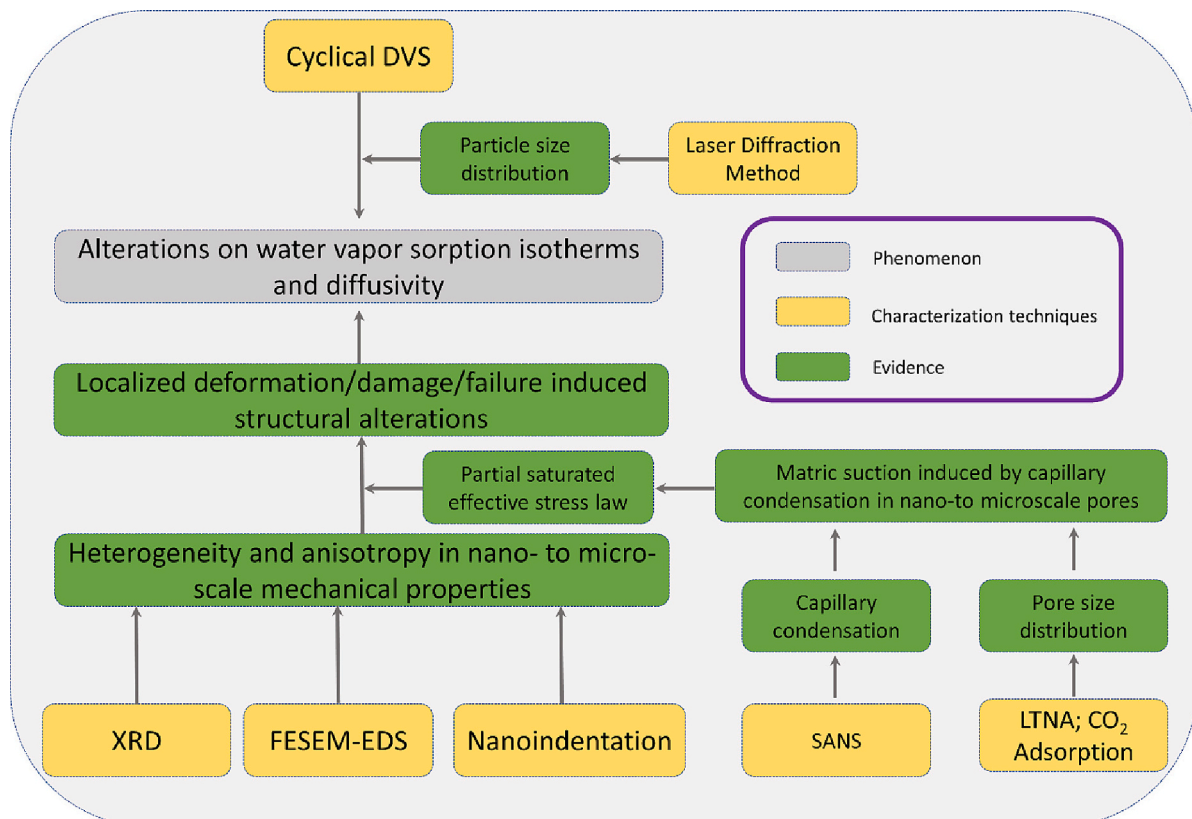

Fig. 10. Mechanism-based understandings of structural alterations in the unsaturated air-water-shale system.
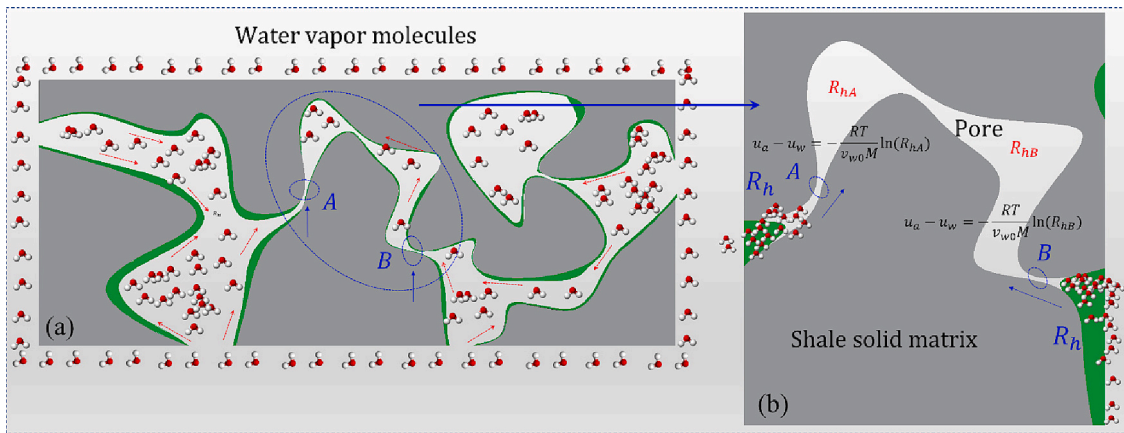
Fig. 11. Illustration of concentrated stress around the nanopores inside the unsaturated shale-water-air system.

classical Mohr-Coulomb criterion and the third term introduces γ as an additional friction angle to capture the contribution of matric suction to the shear strength.

In the case of an unsaturated air-water-shale system, the Mohr's circles corresponding to failure conditions can be plotted in three-dimensions using Eq. (12), as shown in Fig. 12. The three-dimensional plot has the shear stress (τ) as the ordinate and the two stress state variables, $\sigma_t - u_a$ and $u_a - u_w$, as abscissas. The frontal plane represents a saturated case where the matric suction is zero. On the frontal plane, the ($\sigma_t - u_a$) axis reverts to the ($\sigma_t - u_w$) axis since the pore-air pressure becomes equal to the pore-water pressure at saturation. The surface (red plane 'ABCD' in Fig. 12) tangent to the Mohr circles at failure is referred

to as the extended Mohr-Coulomb failure envelope for the unsaturated air-water-shale system. The intersection line between the extended Mohr-Coulomb failure envelope and the frontal plane is the failure envelope for the saturated condition (Fredlund, 1993). The extended Mohr-Coulomb failure envelope may be a planar surface, or it may be somewhat curved depending on the exact values in Eq. (12). In Fig. 12, a planar failure envelope that intersects the shear stress axis, giving a cohesion intercept c', is plotted. The envelope has a slope angle of ϕ' and γ with respect to the $\sigma_t - u_a$ and $u_a - u_w$ axes, respectively. Thus, the cohesion intercept c', and slope angles, ϕ' and γ, are the strength parameters used to relate the shear strength to the stress state variables. The mechanical behavior of the unsaturated air-water-shale system is
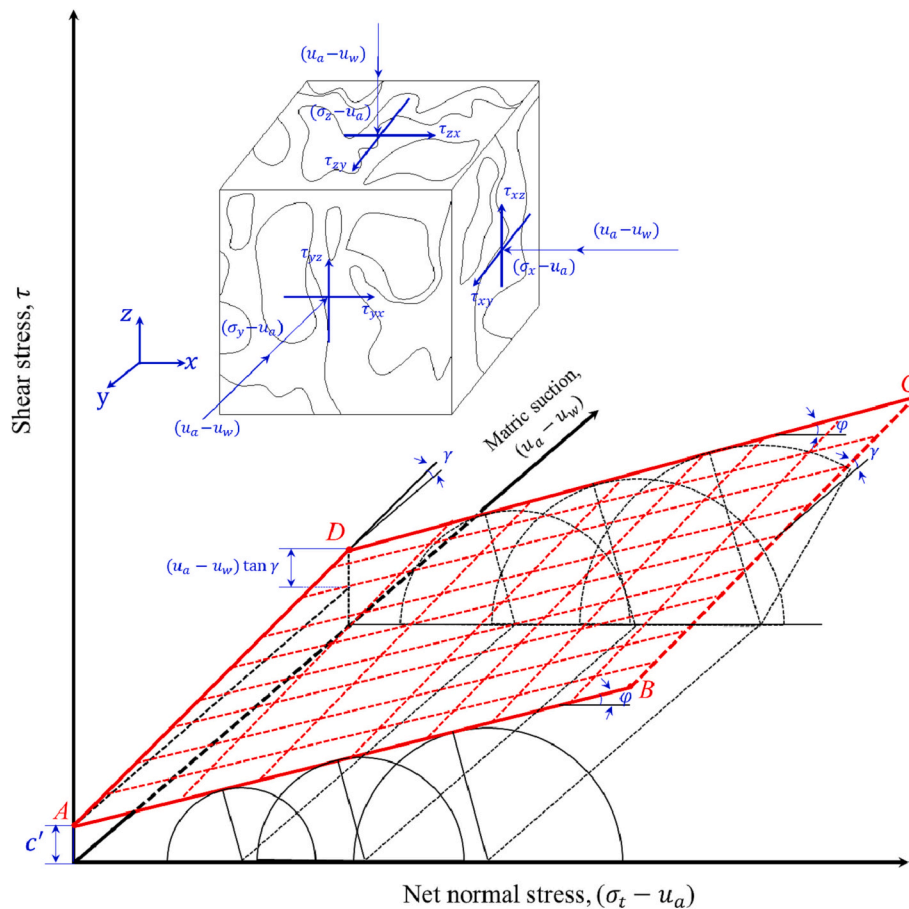

Fig. 12. Extended Mohr-Coulomb failure envelope for the unsaturated air-water-shale system.

affected differently by changes in net normal stress than by changes in matric suction. The increase in shear strength due to an increase in net normal stress is characterized by the friction angle ϕ'. On the other hand, the increase in shear strength caused by an increase in matric suction is described by the angle, γ. In Eq. (12), the effective stress parameter χ for rocks is equal to αS_w (Cheng, 2020), where α is Biot's coefficient and S_w is the water saturation. The water saturation can be estimated based on the water content, and expressed as:

$$m = \frac{m_w}{m_s} = \frac{\rho_w V_w}{\rho_s V_s} = \frac{\rho_w}{\rho_s} \frac{V_w V_p}{V_p V_s} = \frac{\rho_w}{\rho_s} \phi S_w \qquad (13)$$

where ϕ is the effective porosity; ρ_w is the water density; ρ_s is the shale density; m_w is the adsorbed water mass; m_s is the shale mass; V_w and V_s are the volumes of adsorbed water and shale; V_p is the pore volume.

Based on Eq. (7) and (13), the additional friction angle γ to capture the contribution of matric suction to the shear strength can be calculated as:

$$\tan\gamma = \chi \tan\phi' = \frac{m_L R_h}{(R_L + R_h)(1 - cR_h)} \frac{\rho_s}{\phi \rho_w} \tan\phi' \qquad (14)$$

Therefore, the contribution of the matric suction to the shear strength is determined by the additional internal angle of friction, γ (Fig. 12), which is correlated with the relative humidity in Eq. (14). In this study, the nano-porous shale is highly heterogeneous in nano-to-micro-scale mechanical properties with the Young's modulus ranging from ~3.34 GPa to ~38.64 GPa. Based on the partially saturated effective stress law in Eq. (4) and the extended Mohr-Coulomb failure envelope in Fig. 12, the matric suction pressure due to the occurrence of capillary condensation can possibly alter the localized shear strength of nano-porous shale and thereby causes structural failures at those weak regions in nano-porous shale. Based on Eq. (14), in response to the cyclical changes in relative humidity, the water content and effective porosity can passively increase or decrease, and thus the shear strength of the shale can be dynamically altered. The effort to understand air-water-shale interactions raises very complex coupling questions due to the combined elastic deformation field, fluid transport field, and damage evolution field that must all be considered.

5. Summary and conclusion

This study presents a systematic approach to the understanding of shale-water interactions in the unsaturated air-water-shale system. It utilizes a series of techniques XRD, FESEM-EDS, nanoindentation, a laser diffraction method, LTNA and CO_2 adsorptions, *in situ* SANS experiments, and DVS tests to study the cyclical water vapor sorption-induced nanoscale structural changes of shale. Cyclical water vapor sorption tests were conducted on initially dried/water saturated shale powders prepared by a hand-crushing (larger particle size) method and cryogenic ball-milling (smaller particle size) method. Changes in the water vapor sorption isotherms and diffusivity curves among different cycles were quantified and compared. Based on the study, the following major conclusions are drawn:

(1) The techniques including XRD, FESEM-EDS, and nanoindentation provided evidence that the nano-porous shale is highly heterogeneous in nano- to micro-scale mechanical properties with the Young's modulus ranging from ~3.34 GPa to ~38.64 GPa.

(2) The SANS data with elevated relative humidity suggests that the decrease in the scattering contrast between rock solid matrix and pores can be attributed to water capillary condensation—mainly in pores with radii smaller than ~8.3 nm but larger than ~1.25 nm at a relative humidity of ~59%. The capillary condensation continuously takes place in larger pores as the relative humidity increases to ~87%. As the relative humidity decreases from $R_h \sim$ 87% to $R_h \sim$ 38%, the liquified water vapor created by capillary

condensation starts to be gasified in the pores, first in relatively larger pores and then in smaller pores.

(3) Because of capillary condensation in different pores under different relative humidities, an unsaturated air-water-shale system can be formed. Based on the Kelvin equation and the partial saturated effective stress law, it can be asserted that the pore-scale shale structure can be passively altered by pore deformation/failure resulting from the high matrix suction pressure and the heterogeneity in its mechanical properties.

Author statement

Declaration of Competing Interest

Data availability

Data will be made available on request.

Acknowledgement

Appendix A. Supplementary data

Supplementary data to this article can be found online at https://doi.org/10.1016/j.coal.2023.104267.

References

Altabet, Y.E., Haji-Akbari, A., Debenedetti, P.G., 2017. Effect of material flexibility on the thermodynamics and kinetics of hydrophobically induced evaporation of water. Proc. Natl. Acad. Sci. U. S. A. 114, E2548–E2555. https://doi.org/10.1073/pnas.1620335114.

Anderson, R.B., 1946. Modifications of the Brunauer, Emmett and Teller Equation. J. Am. Chem. Soc. 68, 686–691. https://doi.org/10.1021/ja01208a049.

Barsotti, E., Qin, Z., Piri, M., 2021. In situ investigation of fluid-rock interactions at Ångstrom resolution. J. Geophys. Res. Solid Earth 126, 1–17. https://doi.org/10.1029/2020JB021043.

de Boer, J.H., 1953. The Dynamical Character of Adsorption. Published by Oxford University Press/Clarendon Press, London.

Bolton, A.J., Maltman, A.J., Fisher, Q., 2000. Anisotropic permeability and bimodal pore-size distributions of fine-grained marine sediments. Mar. Pet. Geol. 17, 657–672. https://doi.org/10.1016/S0264-8172(00)00019-2.

Brunauer, S., Emmett, P.H., Teller, E., 1938. Adsorption of gases in Multimolecular Layers. J. Am. Chem. Soc. 60, 309–319. https://doi.org/10.1021/ja01269a023.

Charlaix, E., Ciccotti, M., 2010. Capillary condensation in confined media. In: Sattler, K. (Ed.), Handbook of nanophysics: principles and methods, 12. CRC Press, Boca Raton, FL, pp. 1–12.17.

Charrière, D., Behra, P., 2010. Water sorption on coals. J. Colloid Interface Sci. 344, 460–467. https://doi.org/10.1016/j.jcis.2009.11.064.

Cheng, A.H.D., 2020. A linear constitutive model for unsaturated poroelasticity by micromechanical analysis. Int. J. Numer. Anal. Methods Geomech. 44, 455–483. https://doi.org/10.1002/nag.3033.

Choi, J.G., Do, D.D., Do, H.D., 2001. Surface diffusion of adsorbed molecules in porous media: Monolayer, multilayer, and capillary condensation regimes. Ind. Eng. Chem. Res. 40, 4005–4031. https://doi.org/10.1021/ie010195z.

Clarkson, C.R., Solano, N., Bustin, R.M., Bustin, A.M.M., Chalmers, G.R.L., He, L., Melnichenko, Y.B., Radliński, A.P., Blach, T.P., 2013. Pore structure characterization of north American shale gas reservoirs using USANS/SANS, gas adsorption, and mercury intrusion. Fuel 103, 606–616. https://doi.org/10.1016/j.fuel.2012.06.119.

Duan, S., 2018. Equilibrium and kinetics of water vapor adsorption on shale. J. Energy Resour. Technol. 140 (12), 1–10. https://doi.org/10.1115/1.4040530, 122001140.

Dubinin, M.M., Zaverina, E.D., Serpinsky, V.V., 1955. The sorption of water vapour by active carbon. J. Chem. Soc. 1760.

Engelder, T., Cathles, L.M., Bryndzia, L.T., 2014. The fate of residual treatment water in gas shale. J. Unconv. Oil Gas Resour. 7, 33–48. https://doi.org/10.1016/j.juogr.2014.03.002.

Fredlund, D.G., 1991. How negative can pore-water pressures get. Geotech. News 9, 44–46.

Fredlund, D.G., 1993. Soil mechanics for unsaturated soils. Soil Dyn. Earthq. Eng. 12, 449–450. https://doi.org/10.1016/0267-7261(93)90011-f.

Fredlund, D.G., Xing, A., Huang, S., 1994. Predicting the permeability function for unsaturated soils using the soil-water characteristic curve. Can. Geotech. J. 31, 533–546. https://doi.org/10.1139/t94-062.

Fredlund, D.G., Rahardjo, H., Fredlund, M.D., 2012. Unsaturated soil mechanics in engineering practice. Unsaturated Soil Mech. Eng. Pract. 132, 286–321. https://doi.org/10.1002/9781118280492.

Furmaniak, S., Gauden, P.A., Terzyk, A.P., Rychlicki, G., 2008. Water adsorption on carbons - critical review of the most popular analytical approaches. Adv. Colloid Interf. Sci. 137, 82–143. https://doi.org/10.1016/j.cis.2007.08.001.

Ghanbari, E., Dehghanpour, H., 2015. Impact of rock fabric on water imbibition and salt diffusion in gas shales. Int. J. Coal Geol. 138, 55–67. https://doi.org/10.1016/j.coal.2014.11.003.

Gor, G.Y., Huber, P., Bernstein, N., 2017. Adsorption-induced deformation of nanoporous materials - a review. Appl. Phys. Rev. 4, 011303 https://doi.org/10.1063/1.4975001.

Gruener, S., Hofmann, T., Wallacher, D., Kityk, A.V., Huber, P., 2009. Capillary rise of water in hydrophilic nanopores. Phys. Rev. E – Stat. Nonlinear. Soft Matter Phys. 79, 1–5. https://doi.org/10.1103/PhysRevE.79.067301.

Gu, X., Cole, D.R., Rother, G., Mildner, D.F.R., Brantley, S.L., 2015. Pores in marcellus shale: a neutron scattering and FIB-SEM study. Energy Fuel 29, 1295–1308. https://doi.org/10.1021/acs.energyfuels.5b00033.

Guggenheim, E.A., 1966. Applications of Statistical Mechanics, 1st. edition. Clarendon Press.

Honschoten, J.W.V., Brunets, N., Tas, N.R., 2010. Capillarity at the nanoscale. Chem. Soc. Rev. 39, 1096–1114. https://doi.org/10.1039/b909101g.

Langmuir, I., 1916. The constitution and fundamental properties of solids and liquids. Part I. Solids. J. Am. Chem. Soc. 38, 2221–2295.

Liu, A., Liu, S., 2021. Water sorption on coal: effects of oxygen containing function groups and pore structure. Int. J. Coal Sci. Technol. 8, 983–1002. https://doi.org/10.1007/s40789-021-00424-6.

Liu, A., Liu, S., Wang, K., 2022. Moisture retention and multi-mechanistic transport behavior in nanoporous coal. Langmuir 38, 14941–14958. https://doi.org/10.1021/acs.langmuir.2c02701.

Liu, J., Peach, C.J., Spiers, C.J., 2016. Anisotropic swelling behaviour of coal matrix cubes exposed to water vapour: Effects of relative humidity and sample size. Int. J. Coal Geol. 167, 119–135. https://doi.org/10.1016/j.coal.2016.09.011.

Liu, J., Fokker, P.A., Spiers, C.J., 2017. Coupling of swelling, internal stress evolution, and diffusion in coal matrix material during exposure to methane. J. Geophys. Res. Solid Earth 122, 844–865. https://doi.org/10.1002/2016JB013322.

Lu, N., 2008. Is matric duction a stress variable? J. Geotech. Geoenviron. Eng. 134, 899–905. https://doi.org/10.1061/(asce)1090-0241(2008)134:7(899).

Lu, N., Likos, W.J., 2006. Suction stress characteristic curve for unsaturated soil. J. Geotech. Geoenviron. Eng. 132, 131–142. https://doi.org/10.1061/(asce)1090-0241(2006)132:2(131).

Moghadam, A., Vaisblat, N., Harris, N.B., Chalaturnyk, R., 2020. On the magnitude of capillary pressure (suction potential) in tight rocks. J. Pet. Sci. Eng. 190, 107133 https://doi.org/10.1016/j.petrol.2020.107133.

Poulsen, B.A., Shen, B., Williams, D.J., Huddlestone-Holmes, C., Erarslan, N., Qin, J., 2014. Strength reduction on saturation of coal and coal measures rocks with implications for coal pillar strength. Int. J. Rock Mech. Min. Sci. 71, 41–52. https://doi.org/10.1016/j.ijrmms.2014.06.012.

Powles, J.G., 1985. On the validity of the Kelvin equation. J. Phys. A Math. Gen. 18, 1551–1560.

Radliński, A.P., Boreham, C.J., Lindner, P., Randl, O., Wignall, G.D., Hinde, A., Hope, J. M., 2000. Small angle neutron scattering signature of oil generation in artificially and naturally matured hydrocarbon source rocks. Org. Geochem. 31, 1–14. https://doi.org/10.1016/S0146-6380(99)00128-X.

Sang, G., Liu, S., Elsworth, D., Zhang, R., Bleuel, M., 2020. Pore-scale water vapor condensation behaviors in shales: an experimental study. Transp. Porous Media 135, 713–734. https://doi.org/10.1007/s11242-020-01497-8.

Schaefer, C.E., Towne, R.M., Lazouskaya, V., Bishop, M.E., Dong, H., 2012. Diffusive flux and pore anisotropy in sedimentary rocks. J. Contam. Hydrol. 131, 1–8. https://doi.org/10.1016/j.jconhyd.2012.01.005.

Schoen, M., Günther, G., 2010. Phase transitions in nanoconfined fluids: Synergistic coupling between soft and hard matter. Soft Matter 6, 5832–5838. https://doi.org/10.1039/c0sm00440e.

Slatt, R.M., O'Brien, N.R., 2011. Pore types in the Barnett and Woodford gas shales: Contribution to understanding gas storage and migration pathways in fine-grained rocks. Am. Assoc. Pet. Geol. Bull. 95, 2017–2030. https://doi.org/10.1306/03301110145.

Thommes, M., Kaneko, K., Neimark, A.V., Olivier, J.P., Rodriguez-Reinoso, F., Rouquerol, J., Sing, K.S., 2015. Physisorption of gases, with special reference to the evaluation of surface area and pore size distribution (IUPAC Technical Report). Pure Appl. Chem. 87, 1051–1069.

Yang, Q., Sun, P.Z., Fumagalli, L., Stebunov, Y.V., Haigh, S.J., Zhou, Z.W., Grigorieva, I. V., Wang, F.C., Geim, A.K., 2020. Capillary condensation under atomic-scale confinement. Nature 588, 250–253. https://doi.org/10.1038/s41586-020-2978-1.